Significance of hydrothermal reworking for REE mineralization associated with carbonatite: Constraints from in situ trace element and C-Sr isotope study of calcite and apatite from the Miaoya carbonatite complex (China)

Yuan-Can Ying [a], Wei Chen [a,*], Antonio Simonetti [b], Shao-Yong Jiang [a], Kui-Dong Zhao [a]

[a] *State Key Laboratory of Geological Processes and Mineral Resources, Collaborative Innovation Center for Exploration of Strategic Mineral Resources, Faculty of Earth Resources, China University of Geosciences, Wuhan 430074, China*
[b] *Department of Civil and Environmental Engineering and Earth Sciences, University of Notre Dame, Notre Dame, IN 46556, USA*

Abstract

A majority of carbonatite-related rare earth element (REE) deposits are found in cratonic margins and orogenic belts, and metasomatic/hydrothermal reworking is common in these deposits; however, the role of metasomatic processes involved in their formation remains unclear. Here, we present a comprehensive in situ chemical and isotopic (C-Sr) investigation of calcite and fluorapatite within the Miaoya carbonatite complex located in the South Qinling orogenic belt, with the aim to better define the role of late-stage metasomatic processes.

Carbonatite at Miaoya commonly occurs as stocks and dykes intruded into associated syenite, and can be subdivided into equigranular (Type I) and inequigranular (Type II) calcite carbonatites. Calcite in Type I carbonatite is characterized by the highest Sr (up to ∼22,000 ppm) and REE (195–542 ppm) concentrations with slight LREE-enriched chondrite normalized patterns [$(La/Yb)_N$ = 2.1–5.2]. In situ C and Sr isotopic compositions of calcite in Type I carbonatite define a limited range ($^{87}Sr/^{86}Sr$ = 0.70344–0.70365; $\delta^{13}C$ = −7.1 to −4.2 ‰) that are consistent with a mantle origin. Calcite in Type II carbonatite has lower Sr (1708–16322 ppm) and REEs (67–311 ppm) and displays variable LREE-depleted chondrite normalized REE patterns [$(La/Yb)_N$ = 0.2–3.3; $(La/Sm)_N$ = 0.2–2.0]. In situ $^{87}Sr/^{86}Sr$ and $d^{13}C$ isotopic compositions of Type II calcite are highly variable and range from 0.70350 to 0.70524 and −7.0 to −2.2 ‰, respectively. Fluorapatite in Type I and Type II carbonatites is characterized by similar trace-element and isotopic compositions. Both types of fluorapatite display variable trace element concentrations, especially LREE contents, whereas they exhibit relatively consistent near-chondritic Y/Ho ratios. Fluorapatite is characterized by consistent Sr isotopic compositions with a corresponding average $^{87}Sr/^{86}Sr$ ratio of 0.70359, which suggests that fluorapatite remained relatively closed in relation to contamination. The combined geochemical and isotopic data for calcite and fluorapatite from the Miaoya complex suggest that carbonatite-exsolved fluids together with possible syenite assimilation during the Mesozoic metasomatism overprinted the original trace-element and isotopic signatures acquired in the early Paleozoic magmatism. Hydrothermal reworking resulted in dissolution-reprecipitation of calcite and fluorapatite, which served as the dominant source of REE mineralization during the much younger metasomatic activity.

---

* Corresponding author.
E-mail address: wchen@cug.edu.cn (W. Chen).

The results from this study also suggest that carbonatites located in orogenic belts and cratonic edges possess a great potential for forming economic REE deposits, especially those that have undergone late-stage metasomatic reworking.

1. INTRODUCTION

Rare earth elements (REEs) are critical for current industrial applications and indispensable to the development of high technology applications and low carbon energy production approaches. REE resources are dominantly associated with carbonatite complexes, and a small number of the >520 carbonatites worldwide are giant and large deposits that host >50% of all known global rare earth oxide (REO) resources (Weng et al., 2015). The carbonatite-hosted REE deposits are commonly found in cratonic margins or along orogenic belts, e.g., Bayan Obo, Mianning-Dechang and Miaoya in China, Mountain Pass and Bear Lodge in United States, and Cummins Range and Gifford Creek in Australia (Weng et al., 2015; Smith et al., 2016). Multi-stage metasomatic events have rendered deciphering the origin and REE enrichment mechanism of carbonatite-related REE deposits rather complicated. For instance, the Mesoproterozoic Bayan Obo carbonatite was impacted by extensive Paleozoic metasomatism that complicated the interpretation of the petrogenetic history of this world's largest REE deposit; consequently, arguments for its sedimentary or igneous origins have been debated since its discovery about a century ago (Ling et al., 2013; Yang et al., 2017; Song et al., 2018; Yang et al., 2019; Chen et al., 2020). Late-stage, non-magmatic related metasomatism or hydrothermal reworking of carbonatite-associated REE deposits is rather common; other well-known examples include: the Miaoya carbonatite complex in the Qinling Orogen (China; Ying et al., 2017; Çimen et al., 2018; Su et al., 2019; Zhang et al., 2019a,b), the Cummins Range carbonatite complex in the Halls Creek Orogen (Australia; Downes et al., 2014, 2016), the Gifford Creek carbonatite complex along the eastern margin of the Gascoyne Province (Australia; Pirajno et al., 2014; Zi et al., 2017; Slezak and Spandler, 2019, 2020), the Chilwa Alkaline Province located near the Mozambique border (Malawi; Broom-Fendley et al., 2016), the Phalaborwa carbonatite complex on the southern margin of Kaapvaal craton (South Africa; Milani et al., 2017), the Bear Lodge carbonatite near the transition between the Wyoming Archean craton and Proterozoic basement formed during the Trans-Hudson orogeny (United States; Moore et al., 2015; Andersen et al., 2017).

REE enrichment in carbonatite-related deposits is believed to originate from the mantle-derived carbonatite magma, and ensuing magmatic differentiation processes including fractional crystallization and liquid immiscibility, which both play important roles (Chen and Simonetti, 2013; Milani et al., 2017; Yang et al., 2019). An increasing number of field observations, and theoretical and experimental studies have demonstrated that hydrothermal reworking may concentrate REEs to economic levels, regardless of the type of magmatic source (Williams-Jones et al., 2012; Migdisov et al., 2016). However, the role of hydrothermal/metasomatic processes in the formation of carbonatite-associated REE deposits remain poorly understood. It is currently well-accepted that hydrothermal processes can mobilize and redistribute the REEs within igneous systems (Gysi and Williams-Jones, 2013; Migdisov et al., 2016). It has also become apparent that hydrothermal processes can lead to significant spatial fractionation of individual REEs, even within the same deposit (e.g., Bayan Obo; Smith et al., 2000), which relates to the variable uptake of the REEs by hydrothermal fluids (Williams-Jones et al., 2012). Nevertheless, the nature of fluids especially whether they are REE barren or enriched and the behavior of REEs among different mineral phases during metasomatism are currently poorly understood. For example, the nature of the fluids involved in the Paleozoic metasomatic modification in the formation of the giant Bayan Obo deposit remain debated as to whether they were enriched in REEs, and also the behavior of REEs among gangue minerals (e.g., carbonate) and ore minerals (e.g., monazite, bastnäsite, allanite) during metasomatism still remains unclear (Ling et al., 2013; Yang et al., 2017; Liu et al., 2018; Song et al., 2018; Yang et al., 2019; Chen et al., 2020; Liu et al., 2020).

Trace element signatures of calcite and apatite, notably REE contents and patterns, can be used to trace petrogenetic processes affecting carbonatite magmas (Chen and Simonetti, 2013; Broom-Fendley et al., 2016; Chakhmouradian et al., 2016b; Milani et al., 2017; Ranta et al., 2018; Palma et al., 2019; Andersson et al., 2019). Moreover, they are particularly suitable in recognizing metasomatic/hydrothermal reworking of the primary magmatic minerals and tracing the origin, chemistry, and evolution of fluids in metasomatic ore-forming settings (Li and Zhou, 2015; Harlov et al., 2016; Ranta et al., 2018; Palma et al., 2019; Andersson et al., 2019). The Miaoya carbonatite complex located in the Qinling orogenic belt hosts the second largest REE-Nb deposit in China (Fig. 1). In this study, we present a combined petrographic, chemical, and Sr and C isotopic investigation of calcite and fluorapatite from this deposit. The main aim is to identify the role of late-stage, non-magmatic related metasomatic processes or hydrothermal reworking in the generation of REE deposits. The newly obtained in situ chemical and isotopic data for both calcite and fluorapatite from the Miaoya REE-Nb deposit serve as tracers of the REE behavior in late-stage metasomatic processes.
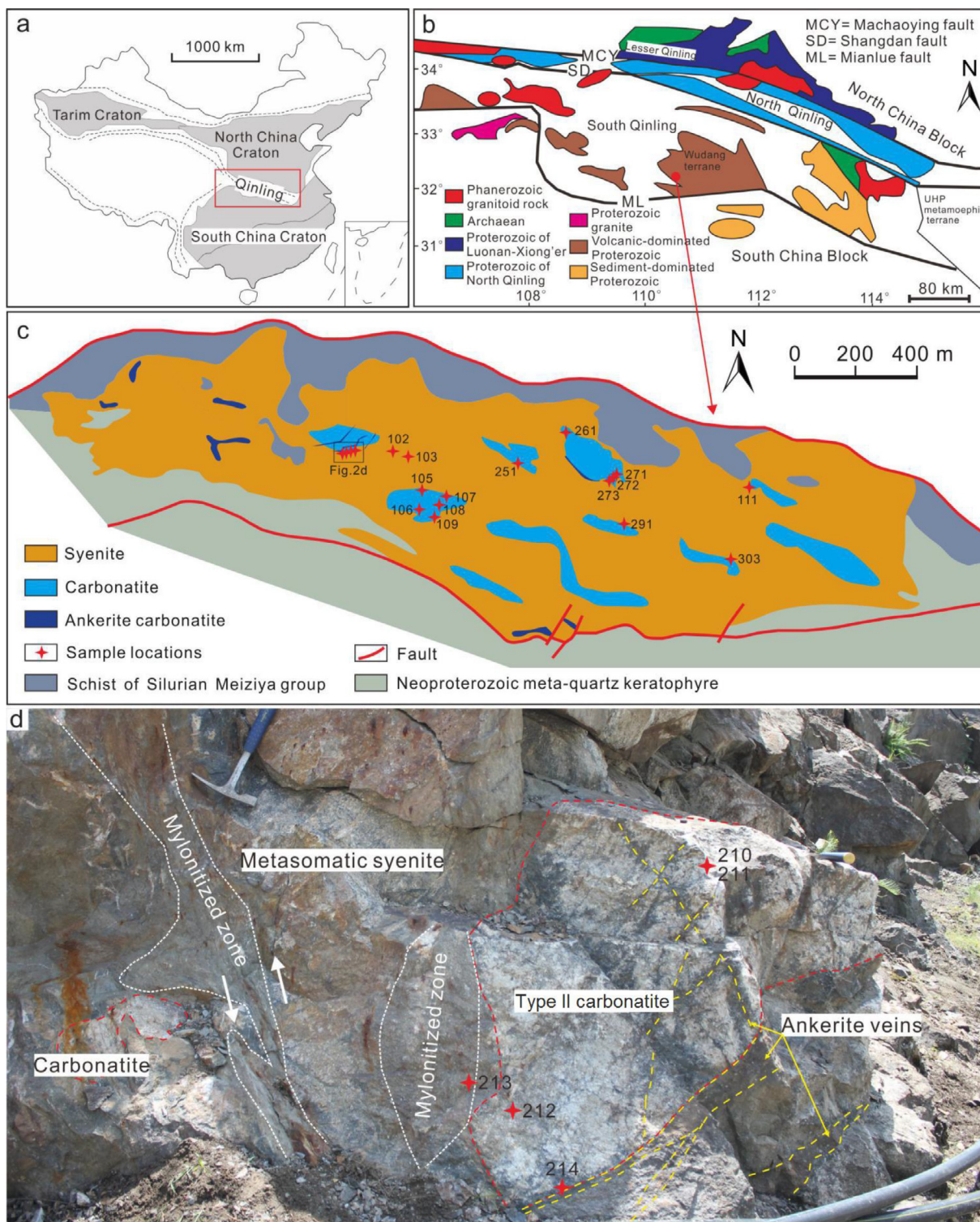
Fig. 1. Geological map and field outcrop picture for the Miaoya carbonatite complex. (a) Map of China with the major tectonic domains highlighted. (b) Simplified geological map of the Qinling orogen and its tectonic division. (c) Simplified geological map of the Miaoya complex, modified from Ying et al. (2017). (d) Outcrop picture shows the intrusive contact between the carbonatite lens and syenite. Samples collected for the investigation are shown in (c) and (d). Number labels within outcrop photo correspond to the sampling locations of the carbonatite lens from center to edge.

2. GEOLOGICAL SETTING

The Qinling orogenic belt formed during the collision between the North China Block (NCB) and the South China Block (SCB) in central China. The orogen is subdivided into North Qinling and South Qinling belts by the Shangdan suture (Fig. 1a, b). This suture formed as the result of the Silurian to early Devonian subduction of the South Qinling Terrane beneath the North Qinling plate (Dong et al., 2011). The Mianlue Ocean separated the South Qinling orogenic belt from the SCB during the Devonian to early Triassic, and the closure of the Mianlue Ocean led to the final collision of the North China and South China Blocks during the early-middle Triassic (Dong et al., 2011; Wu and Zheng, 2013).

The Miaoya carbonatite complex is located at the southwestern margin of the Wudang Terrane along the southern edge of the South Qinling orogen and close to the Mianlue suture (Fig. 1b). The complex consists of both carbonatite and syenite and hosts abundant REE and Nb mineralization, representing the second largest REE-Nb deposit in China (Xu et al., 2014, 2015; Su et al., 2019). The carbonatite and alkaline syenite were emplaced along the E-W-trending contact between the meta-quartz keratophyre of the Neoproterozoic Yaolinghe Group (685 ± 5 Ma, Ling et al., 2007) and the schist from the lower Silurian Meiziya Group, which covers an area of ~6.5 km^2 (Fig. 1c). At Miaoya, carbonatite was intruded into the associated syenite as stocks and dikes (Fig. 1c, d), with a zircon Th-Pb age for the carbonatite of 426.5 ± 8.0 Ma, which is approximately 16 million years younger than the associated syenite (442.6 ± 4.0 Ma; Ying et al., 2017). Similar zircon U-Th-Pb ages for both the carbonatite and syenite have been reported by Zhu et al. (2016) and Su et al. (2019). The ages for a series of early Paleozoic alkaline and ultramafic–mafic magmatic rocks have been reported in this region, including the Shaxiongdong carbonatite and syenite (441.8 ± 2.2 Ma; Chen et al., 2018), the Tianbao trachyte (431 ± 2.6 Ma; Wan et al., 2016), the Lang'ao trachyte (433 ± 2.5 Ma; Wang, 2014), and the Ziyang-Lang'ao mafic intrusive rocks (438 ± 4 Ma; Xiang et al., 2016). The petrogenesis and geodynamic setting of ultramafic–mafic dikes and alkaline complexes in the South Qinling orogenic belt remain controversial, but it is generally agreed that a significant crustal extensional regime in the early Paleozoic generated these magmatic rocks (Zhang et al., 2007; Wang et al., 2017). The Triassic closure of the Mianlue Ocean resulted in metamorphism and hydrothermal activity on a large scale in the South Qinling orogen (Wu and Zheng, 2013). Triassic metasomatism has been recorded in the Miaoya carbonatite complex based on U-Th-Pb ages of monazite, bastnäsite and columbite, including ages of 233.6 ± 1.7 Ma (Xu et al., 2014) and 238.3 ± 4.1 Ma (Ying et al., 2017) for monazite in carbonatite, 243.1 ± 2.5 Ma for monazite in syenite (Ying et al., 2017), 205.8 ± 3.6 Ma for bastnäsite in carbonatite (Zhang et al., 2019b), and 232.8 ± 4.5 Ma for columbite in carbonatite (Ying et al., 2017). Thus, the magmatic-metasomatic evolution of the Miaoya carbonatite complex is closely related to the two major tectonic episodes that occurred within the South Qinling orogen.

3. SAMPLES AND METHODS

Petrographic examination of the samples investigated in this study was conducted using optical microscopy and scanning electron microscopy equipped with an energy-dispersive X-ray spectrometer at the State Key Laboratory of Geological Processes and Mineral Resources (GPMR), China University of Geosciences (Wuhan). Optical CL (cathodoluminescence) imaging was carried out using a Leica DM 2700P microscope coupled to a Cambridge Image Technology LTD (CITL) MK5-2CL system. The CITL system was operated at 12 kV accelerating voltage and 350 mA current. Back-scattered electron (BSE) images were captured using a high-definition backscattered electron detector connected to a Zeiss Sigma 300 field emission scanning electron microscope.

In situ chemical analyses of calcite and fluorapatite were performed using a RESOlution 193 nm laser ablation system coupled to a Thermo iCAP-Q inductively coupled plasma mass spectrometer (LA-ICP-MS) at GPMR, China University of Geosciences (Wuhan). Calcite and fluorapatite were ablated using a 32 μm spot size, 8 Hz repetition rate, and energy density of ~4 J/cm^2. Each spot analysis incorporates approximately 30 s of background acquisition and 40 s of sample data acquisition. In this study, we adopted multiple reference materials (NIST 612, BIR-1G, BCR-2G and BHVO-2G) as external standards without the use of an internal standard for concentration determination (Liu et al., 2008). The analytical uncertainty is better than 5% for REEs and 10% for the remaining elements (1 s level; Chen et al., 2011). Off-line selection and integration of background and analytical signals, and time drift correction and quantitative calibration were performed using ICPMS-DataCal 10.7 (Liu et al., 2008).

In situ U-Pb dating of fluorapatite was conducted using the same instrument configuration as described above for elemental determinations. The analytical protocol follows that described by Chen and Simonetti (2013). Samples were ablated using a spot size of 50 μm, a repetition rate of 8 Hz, and energy density of 5–6 J/cm^2. A matrix-matched external standard (the Madagascar apatite, MAD) was used to correct for the U/Pb fractionation and instrumental mass discrimination (Thomson et al., 2012). The data reduction was carried out using an in-house excel-based program developed by Chen and Simonetti (2013). Tera-Wasserburg diagrams and weighted mean ^{206}Pb/^{238}U ages were produced using Isoplot v3.0 (Ludwig, 2003).

Carbon and oxygen isotopic compositions of separated calcite grains were determined at GPMR, China University of Geosciences (Wuhan). Calcite collected from hand specimens was pulverized to ~200 mesh powders for C-O isotopic analyses. Calcite powders were reacted with anhydrous orthophosphoric acid at 50 °C. Evolved CO_2 was purified, then its C and O isotopic compositions were measured on a Finnigan MAT-251 isotope ratio mass spectrometer. Isotopic compositions are reported relative to the

Vienna Pee Dee Belemnite standard (V-PDB) for $\delta^{13}C$ and Vienna Standard Mean Ocean Water (V-SMOW) for $\delta^{18}O$. The analytical uncertainty is better than 0.15‰ and 0.20‰ (2 s) for C and O isotope ratio measurements, respectively.

In situ Sr isotopic analyses of calcite and fluorapatite were done using a RESOlution 193 nm laser ablation system coupled to a Nu Plasma II MC-ICP-MS at GPMR, China University of Geosciences (Wuhan). In situ Sr isotope measurements involve corrections of critical spectral interferences that include Kr, Rb and bivalent REEs (Ramos et al., 2004). Instrumental operating conditions and detailed correction protocols are described in Ramos et al. (2004) and Chen et al. (2018). A modern-day coral (Qingdao) served as an external, in-house standard, which is used to evaluate the reliability of analytical accuracy employed here. In this study, repeated analysis of the coral yielded an average $^{87}Sr/^{86}Sr$ ratio of 0.70917 ± 0.00003 (2σ, n = 30), which is similar to the value of 0.70923 ± 0.00002 obtained by TIMS (Chen et al., 2018).

The same instrument configuration was adopted for the determination of in situ carbon isotope compositions of calcite as that employed for the Sr isotope analyses at GPMR. The detailed analytical procedures for in situ C isotope measurements of calcite are described in Chen et al. (2017). A standard-sample bracketing (SSB) method was used to correct for instrumental mass bias with the Oka153 calcite employed as the external standard. Both samples and standards were ablated with laser beam diameters of 130–193 μm, repetition rate of 8 Hz, and

energy density of 4 J/cm². The analytical uncertainty is better than 0.25‰ (1 s) for C isotopes based on repeated analyses of the Oka153 calcite (Chen et al., 2017).

4. MINERALOGY AND PARAGENESIS

The Miaoya carbonatites can be grouped into equigranular and inequigranular calcite carbonatites based on their texture (Figs. 2 and 3). The former (Type I) consist of relatively homogeneous, medium-grained calcite (~500 μm; Fig. 2), whereas the latter (Type II) are composed of calcite with variable grain sizes (20 μm–2 cm; Fig. 3).

Type I carbonatite is composed of medium-grained calcite with variable proportions of fluorapatite, biotite, albite, quartz, and monazite (e.g., samples MY105, MY107 and MY271; Fig. 2). Calcite grains are euhedral to subhedral, or referred as mosaic texture in Chakhmouradian et al. (2016a) (Fig. 2b). Fluorapatite occurs as individual subhedral, equant to elongate crystals (<1000 μm long) disseminated in the dominant calcite (Fig. 2b–f). Some fluorapatite displays a patchy texture with various zonation and pink, mauve, and yellow CL colors (Fig. 2c, f). The dominant REE mineral in Type I carbonatite is monazite-(Ce), which commonly occurs along fluorapatite rims and fractures, or as aggregates disseminated in calcite (Fig. 2b, d). Other accessory minerals identified in Type I carbonatite include bastnäsite-(Ce), parisite-(Ce), allanite-(Ce), zircon, pyrite, columbite, betafite, and Nb-bearing rutile.
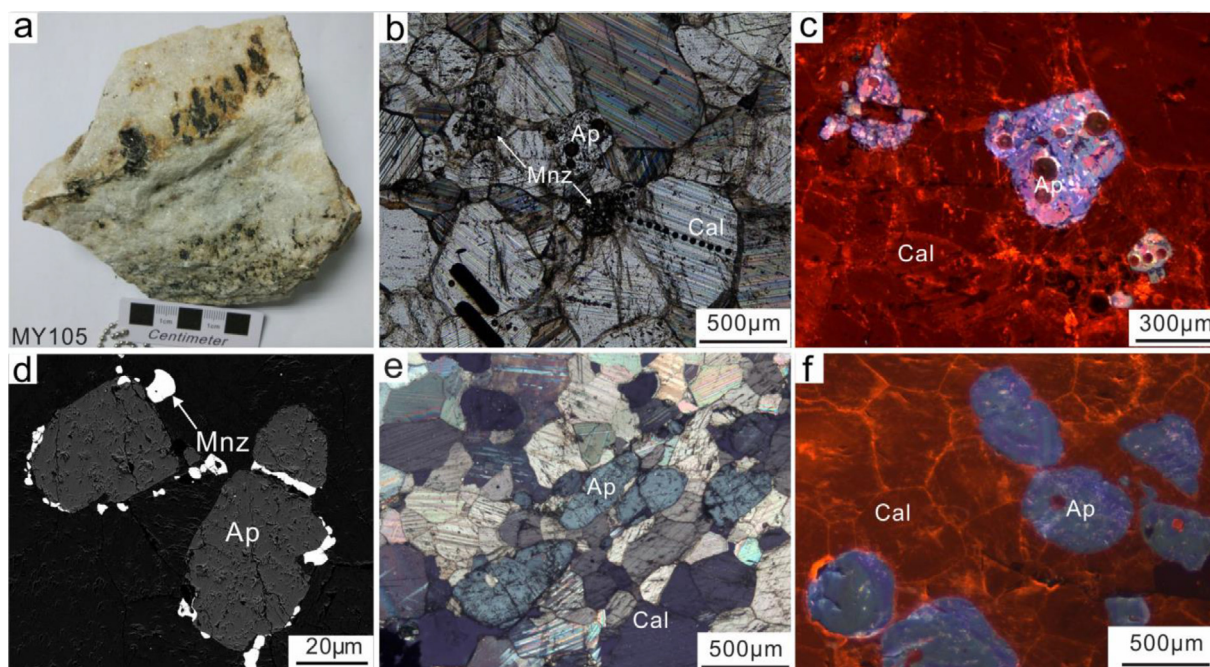

Fig. 2. Petrographic images of Type I carbonatite. (a) Hand specimen of Type I carbonatite. (b and c) Photomicrograph and CL images of Type I carbonatite with minor fluorapatite and accessory monazite. (d) BSE image illustrating monazite occurring in the rim and fracture of fluorapatite. (e–f) Euhedral to subhedral fluorapatite disseminated within Type I carbonatite. Abbreviations: fluorapatite (Ap), calcite (Cal), monazite-(Ce) (Mnz).
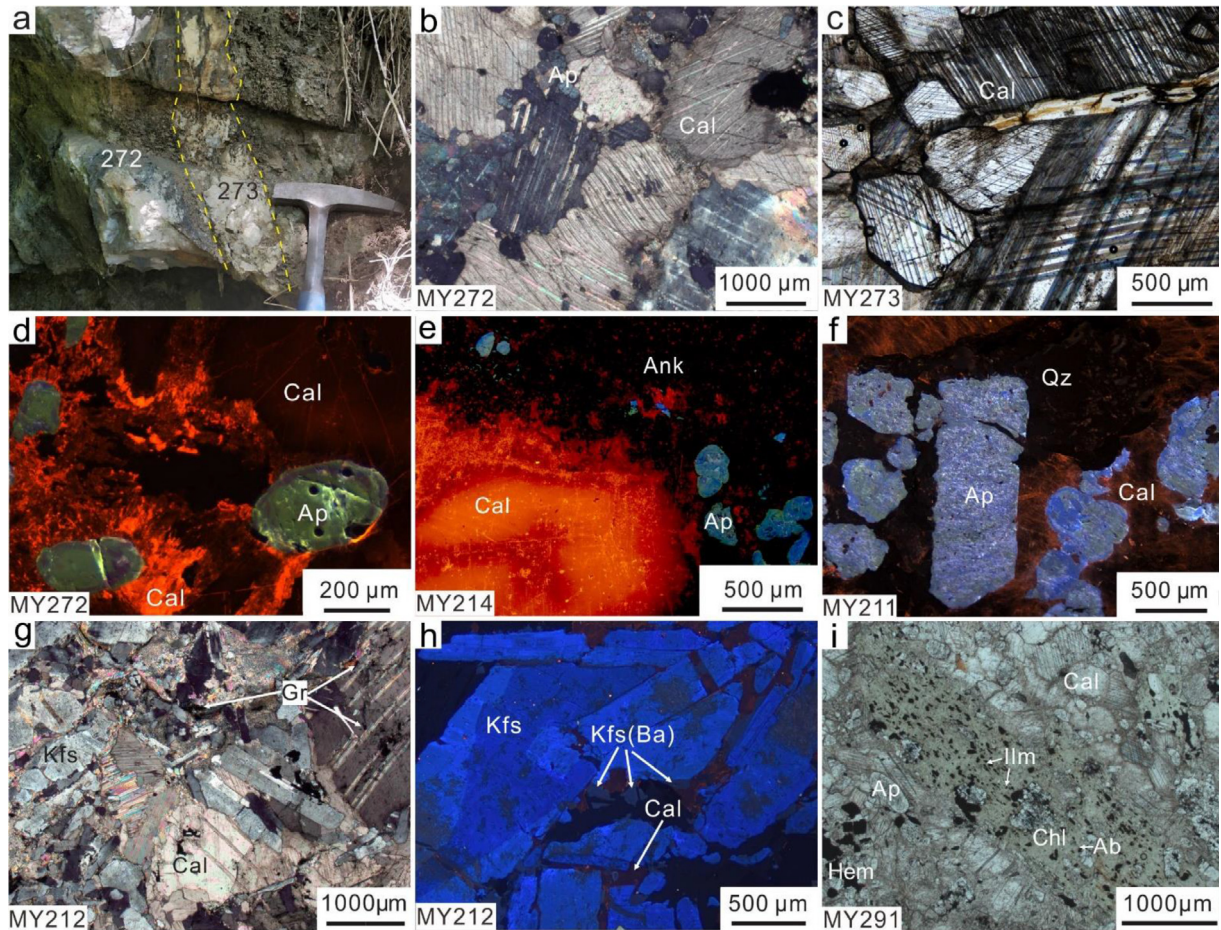
Fig. 3. Field photos and petrographic images of Type II carbonatite. (a–c) Inequigranular calcite carbonatite vein (Sample 273) crosscutting the other carbonatite (Sample 272). Medium-grained subtly elongate calcite in carbonatite sample 272 is characterized by bent twin lamellae; sample 273 consists of a variety of calcite with grain size vary from 200 um to 2 cm. (d–f) CL images of Type II carbonatite within the carbonatite lens as shown in Fig. 1d. (d) Calcite near ankerite veins showing flame-like zoning. (e) Fine-grained calcite forming veins that intersect coarse-grained calcite, referred as "core-and-mantle" aggregates in Chakhmouradian et al. (2016a). (f) Fluorapatite displayinng patchy textures of blue to green color variation and ankerite does not show luminescence. (g) Minor interstitial graphite occurring in calcite. (h) K-feldspar within Type II carbonatite, with rims altered to Ba-rich feldspar. (i) Some biotite in Type II carbonatite altered to chlorite, the exsolution of ilmenite in chlorite is common. Abbreviations: ankerite (Ank), albite (Ab), chlorite (Chl), Gr (graphite), hematite (Hem), K-feldspar (Kfs), ilmenite (Ilm), quartz (Qz); the rest are consistent with those in Fig. 2.

Type II carbonatite consists of inequigranular calcite with grain sizes varying from fine- to coarse-grained (20 μm to 2 cm; Fig. 3). Medium-grained calcite (200 to 2000 μm) is dominant in Type II carbonatite, and commonly displays irregular and serrated grain boundaries (Fig. 3b, d). Bent twin lamellae in some calcite grains (Fig. 3b) indicate a certain degree of ductile deformation of the carbonatite. Carbonatite sample 273 consists of dominantly extremely coarse-grained calcite with grain size >1 cm and occurs as a late-stage vein cutting the earlier-formed carbonatite (Sample 272; Fig. 3a, c). Medium- to coarse-grained calcite generally displays a lighter red core and a darker margin in the CL image (Fig. 3e). In addition to calcite, common constituents in Type II carbonatite are fluorapatite, orthoclase, quartz, albite, microcline, and biotite (Fig. 3). Fluorapatite in Type II carbonatite is texturally complex and shows variety of mauve, blue, green, and yellow colors in CL images (Fig. 3d–f). Biotite is transformed

into chlorite in some carbonatite samples and exsolution of ilmenite in chlorite is common (Fig. 3i); other accessory minerals within Type II carbonatite include monazite-(Ce), bastnäsite-(Ce), parisite-(Ce), columbite, allanite-(Ce), zircon, pyrite and fluorite (Fig. 3).

Type II carbonatites are characterized by the dominant monazite mineralization (Fig. 4a, b) and accompanied by other REE minerals, such as parisite-(Ce) and bastnäsite-(Ce) (Fig. 4c–f). Fine-grained monazite-(Ce) generally occurs disseminated in calcite or as aggregates in close association with fluorapatite, albite, and quartz (Fig. 4a, b). Monazite aggregates can also be found as micro-veins filled along the fractures in syenite (Fig. 4i). Parisite-(Ce) intergrown with bastnäsite-(Ce) is common, and fluorocarbonates generally occur together with biotite, pyrite, calcite, and ankerite (Fig. 4c–f). Allanite-(Ce) occurs in association with ilmenite, biotite, albite, and ankerite (Fig. 4g). Similar REE mineralization consisting of monazite-
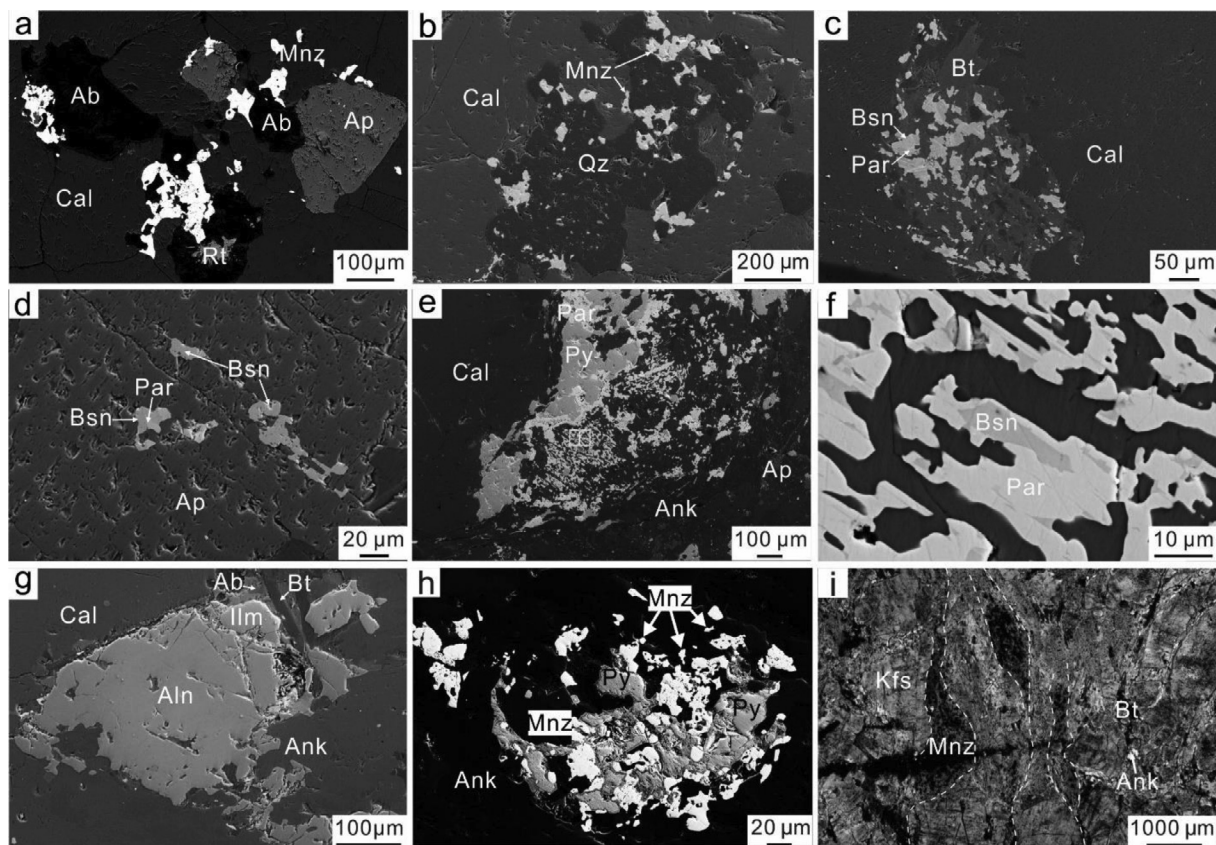
Fig. 4. Typical REE mineralization associated with Type II carbonatite. (a) Monazite in association with albite and fluorapatite. (b) Monazite associated with quartz. (c) Bastnäsite and parisite intergrown with biotite. (d) Bastnäsite and parisite included in fluorapatite. (e) Bastnäsite and parisite intergrown with pyrite occurring adjacent to margin of calcite and ankerite. (f) Magnified view of the box area in (e), showing the intergrowth of bastnäsite and parisite. (g) Minor subhedral allanite grains disseminated within Type II carbonatite in association with biotite, albite and ilmenite. (h) Monazite closely intergrown with pyrite in ankerite veins. (i) Fine-grained monazite aggregates as micro-veins in syenite. Abbreviations: allanite (Aln), bastnäsite (Bsn), biotite (Bt), parisite (Par), pyrite (Py); the rest are the same with those in Figs. 2 and 3.

fluorocarbonate can be identified in the late-stage, fine-grained ferrocarbonatite veins (Fig. 4h).

A typical Type II carbonatite is represented by a road-side outcrop (Fig. 1d), which contains a carbonatite lens that intruded into syenite. The center of the carbonatite lens consists of medium- to fine-grained calcite, with minor fluorapatite, monazite-(Ce), albite, K-feldspar, ilmenite, bastnäsite-(Ce), parisite-(Ce), rutile, columbite, allanite-(Ce), fluorite, and sulfide (Fig. 3f; Samples MY210 and MY211). Samples retrieved from the margin of the carbonatite indicate assimilation of the surrounding syenite (Fig. 3g, h; Sample MY212), and these consist predominantly of anhedral calcite and K-feldspar, and distortion of twin lamellae can be observed in some calcite (Fig. 3g). Polycrystalline aggregates dominated by microgranular silicate and carbonate minerals were injected into fractures, and locally, mixed with graphite probably originating from the schist of the Meiziya Group (Fig. 3g). K-feldspar typically displays blue and deep blue cathodoluminescence, and the cores are commonly turbid with the rims altered to Ba-rich K-feldspar (i.e., hyalophane; Fig. 3h). Some syenite underwent deformation at the outcrop scale. The late-stage ferrocarbonatite veins display rusty colors due to

weathering, and commonly consist of fine-grained ankerite with varying proportions of monazite-(Ce), bastnäsite-(Ce), parisite-(Ce), allanite, rutile, and sulfides (Fig. 4h).

5. RESULTS

5.1. Chemical compositions of calcite and fluorapatite

Chemical compositions of calcite and fluorapatite in Type I and Type II carbonatites at Miaoya are reported in the Supplementary Material (SM) Tables 1 and 2. Calcite in Type I carbonatite is characterized by elevated Sr concentrations (6725–22046 ppm), and relatively low FeO, MnO, and MgO contents (0.38–1.84 wt.%, 0.29–0.60 wt.% and 0.19–0.91 wt.%, respectively). This calcite shows an appreciable variation in REE contents (195–542 ppm), and is characterized by negatively sloped chondrite normalized REE patterns with the $(La/Yb)_N$ and $(La/Sm)_N$ ratios in the range of 2.1–5.2 and 1.0–1.9, respectively (SM Table 1; Fig. 5a, c). Fluorapatite in Type I carbonatite displays variable trace element concentrations, especially REE contents. It is characterized by strong variations in LREE contents (977–9794 ppm) and degree of
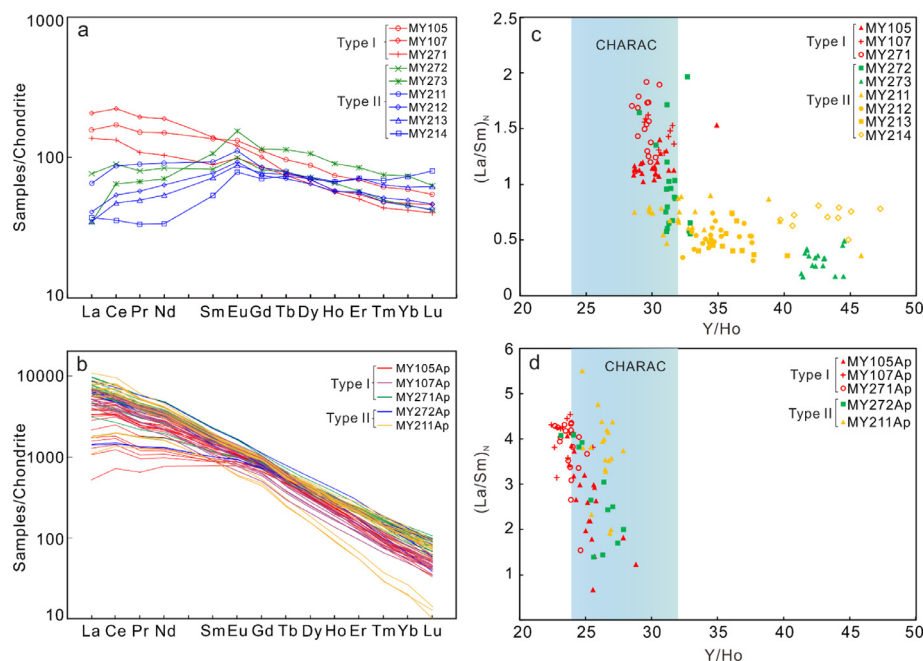
Fig. 5. Trace element compositions of fluorapatite and calcite from the Miaoya carbonatite complex. Chondrite-normalized REE patterns of calcite (a) and fluorapatite (b) from Type I and II carbonatites, and $(La/Sm)_N$ vs. Y/Ho plots of calcite (c) and fluorapatite (d). Chondrite values are from McDonough and Sun (1995), and the CHARAC interval of Y/Ho ratios in (c) and (d) is taken from Bau (1996).

LREE-enrichment, as can be seen from the chondrite normalized REE patterns with $(La/Yb)_N$ and $(La/Sm)_N$ ratios of 9–100 and 0.7–4.5, respectively (SM Table 2; Fig. 5b). The variable LREE contents can be attributed to monazite crystallization since the latter occurs as inclusions or along rims and fractures in the fluorapatite (Fig. 2d). In general, fluorapatite zones adjacent to monazite have lower contents of LREEs and Th. In addition, fluorapatite within Type I carbonatite is enriched in Sr (on average, 9922 ppm) and depleted in U and Th (on average, 3.2 and 39 ppm, respectively).

Calcite in Type II carbonatite contains generally higher contents of MnO and FeO (0.22–3.51 wt.% and 0.26–4.04 wt.%, respectively), but lower Sr and REE abundances (1708–16322 ppm and 67–311 ppm, respectively) compared to that in Type I carbonatite (SM Table 1). Trace element compositions of calcite in Type II carbonatite show large variations (SM Table 1; Fig. 5a, c), particularly in relation to chondrite normalized REE patterns. Their $(La/Yb)_N$ and $(La/Sm)_N$ values range from 0.2 to 3.3 and from 0.2 to 2.0, respectively (Fig. 5a; SM Table 1). In general, they display convex-upward chondrite normalized REE patterns that peak at Eu, with depleted LREE signatures compared to those for calcite in Type I carbonatite (Fig. 5a). Calcite in Type II carbonatite is characterized by a large variation in Y/Ho ratios (29–47), which deviate from the chondritic value, and are much higher compared to the more consistent Y/Ho ratios (~30) in calcite from the Type I carbonatite (SM Table 1; Fig. 5c; Bau, 1996). Of note, fluorapatite in Type II carbonatite generally shows similar trace element compositions compared to that in Type I carbonatite (Fig. 5b, d; SM Table 2). It is characterized by a

negatively sloped REE chondrite normalized pattern with variable LREE-enrichments (Fig. 5b). $(La/Sm)_N$ ratios of fluorapatite in Type II carbonatite define a similar range of 1.2–5.5 compared to the values measured in Type I carbonatite, and its Y/Ho ratios also show a limited range of near-chondritic values (23–28; Fig. 5d; Bau, 1996).

5.2. Chemical variations recorded in calcite within the carbonatite lens

Calcite in the Type II carbonatite samples collected from the primary outcrop (Fig. 1d) has been investigated in more detail (Fig. 6). Calcite in the center of the carbonatite lens (samples MY210 and MY211; Fig. 1d) is characterized by relatively high Sr contents (on average, 9676 ppm) and variable FeO contents (0.41–4.04 wt.%). Coarse- and fine-grained calcite samples within the central carbonatite display different chemical compositions, as the latter has higher contents of Mg, Fe, and Mn but lower concentrations of Sr and REE, especially LREEs (SM Table 1; Fig. 7). The coarse-grained calcite core from the central carbonatite is characterized by lower MgO, FeO, and MnO contents, and higher concentrations of Sr and REE in contrast to the rim (Fig. 6a and 7; SM Table 1). The chondrite normalized REE patterns show convex-upward trends and peak at Eu, which is typical for calcite in Type II carbonatite at Miaoya (Fig. 6d). At the margin of the carbonatite lens (sample MY212; Fig. 1d and 6b), calcite is characterized by higher MnO contents (on average, 0.74 wt.%) and lower Sr abundances (on average, 3370 ppm) than calcite at the center of the lens (SM Table 1). Calcite in the margin of the carbonatite lens also displays in general lower REE
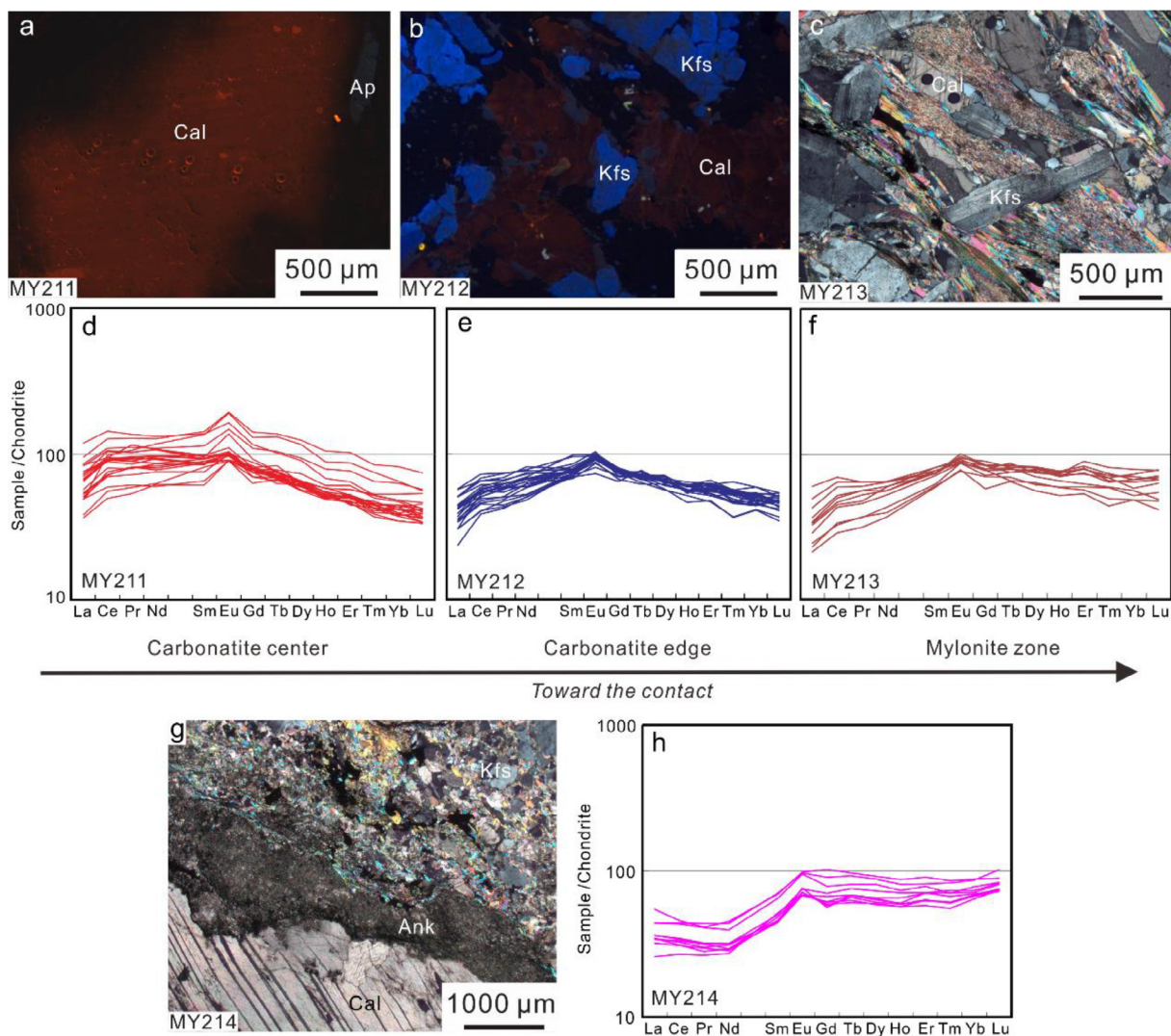
Fig. 6. Chondrite-normalized REE patterns of calcite from center to edge within the carbonatite lens. Sample locations can be found in Fig. 1d. Chondrite values are from McDonough and Sun (1995).

contents compared to calcite at the center (on average, 153 and 201 ppm, respectively; Fig. 6d, e).

Calcite in the deformed syenite (sample MY213; Fig. 1d and 6c) is rare and characterized by high MnO, MgO, and FeO contents (1.90 wt.%, 1.14 wt.% and 2.80 wt% on average, respectively) and relatively low Sr abundances (on average, 4162 ppm; Fig. 6f; SM Table 1). REE contents and patterns for this calcite are similar to those for samples located at the margin of the carbonatite, whereas the former is characterized by relatively higher HREE contents (Fig. 6e, f). Calcite in carbonatite (sample MY214; Fig. 6g) at the contact with ankerite veins shows similar Mn, Mg, Fe, and Sr contents relative to calcite within the deformed syenite (SM Table 1). The former contains the lowest LREE levels (on average, 49 ppm) and shows even greater HREE enrichment (on average, 52 ppm; SM Table 1), and displays LREE-depleted chondrite normalized REE patterns with (La/Yb)$_N$ values in the range of 0.4–0.6 (Fig. 6h). Accurate assessment of the REE

contents within ankerite is difficult due to the fact that it contains numerous REE mineral inclusions, such as monazite, bastnäsite, and parisite.

5.3. In situ U-Pb age dating of fluorapatite

Fluorapatite is ubiquitous in the Miaoya carbonatite, and trace element analyses indicate that it is characterized by low contents of U (on average, 4.0 ppm) that hinder acquisition of high-quality U-Pb dating results (SM Table 2). In general, fluorapatite contains high contents of common Pb with U/Pb ratios < 10 (SM Table 2). Fluorapatite with relatively higher U contents from Type I and Type II carbonatites was analyzed using LA-ICP-MS, and U-Pb dating age results are reported in SM Table 3 and shown in Fig. 8. The calculated $^{206}Pb/^{238}U$ ages associated with U/Pb ratios <5 yield geologically insignificant ages (up to 800 Ma), which is an analytical artefact related to an inaccurate common Pb correction. Thus, only
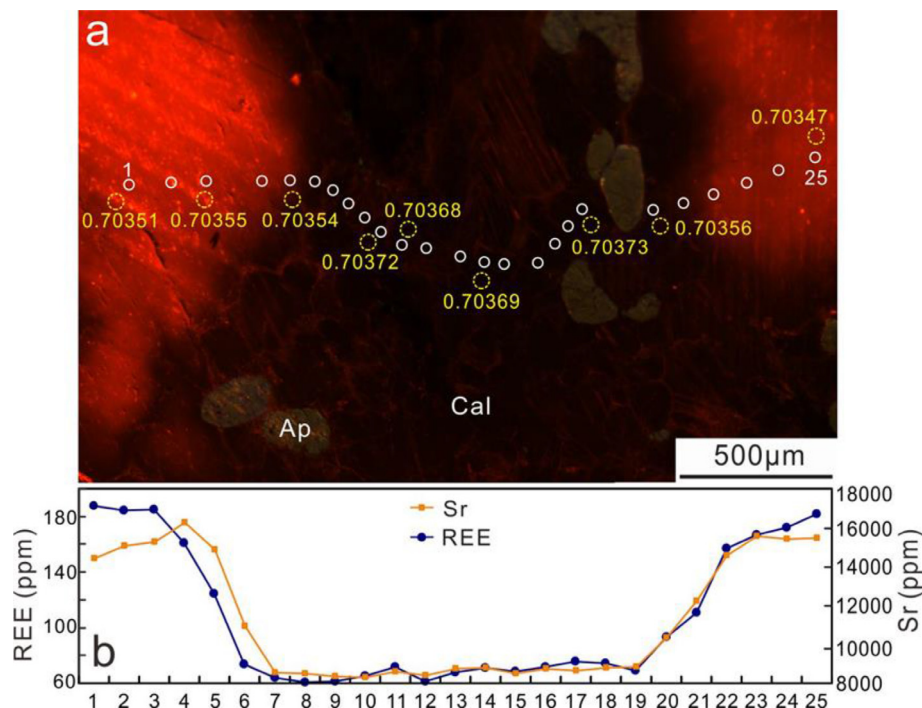
Fig. 7. In situ trace element and Sr isotopic compositions of fine-grained and coarse-grained calcite from the center of carbonatite lens. The white circles represent in situ trace element analytical spots, whereas the yellow circles represent locations of $^{87}Sr/^{86}Sr$ measurements.

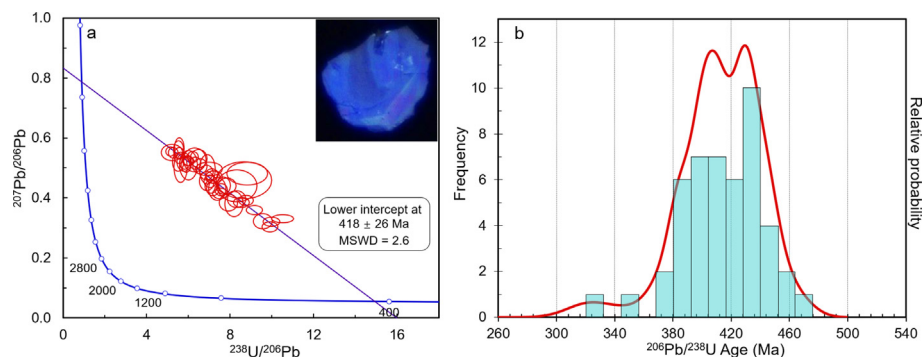
Fig. 8. The Tera-Wasserburg concordia plot (a) and relative probability diagram (b) for $^{206}Pb/^{238}U$ ages of fluorapatite from the Miaoya carbonatite.

analyses characterized by $^{238}U/^{206}Pb$ ratios >5 are reported, and these yield a lower intercept age of 418 ± 26 Ma in a Tera-Wasserburg plot (Fig. 8a). The y-intercept corresponds to a $^{207}Pb/^{206}Pb$ ratio of 0.834 and represents the best estimate for the composition of the common Pb component, and the resulting common Pb-corrected $^{206}Pb/^{238}U$ ages are plotted in a relative frequency plot (Fig. 8b). These calculated ages vary from 321 Ma to 467 Ma with a crudely bimodal data distribution and peak at 430 Ma and 408 Ma (Fig. 8b).

5.4. In situ Sr isotope composition of calcite and fluorapatite

The calculated $^{87}Rb/^{86}Sr$ ratios for both calcite and fluorapatite are extremely low (SM Tables 1 and 2), and there-fore the measured $^{87}Sr/^{86}Sr$ ratios obtained for individual grains can be considered as representing their initial Sr isotopic compositions due to the negligible radiogenic contribution of ^{87}Sr (SM Table 4; Fig. 9). The Sr isotopic composition of a feldspar separate from the syenite is also listed in SM Table 4.

The Sr isotopic compositions of calcite from the different samples investigated here show a large variation between 0.70344 and 0.70524, whereas those of fluorapatite exhibit a more limited range (0.70347–0.70389) with an average of 0.70359 (SM Table 4; Fig. 9). $^{87}Sr/^{86}Sr$ ratios of calcite from Type I carbonatite (0.70344 to 0.70364) are relatively uniform and consistent with the Sr isotope ratios of the associated fluorapatite (0.70350–0.70356). In contrast, Sr isotopic compositions of calcite from Type II carbonatite
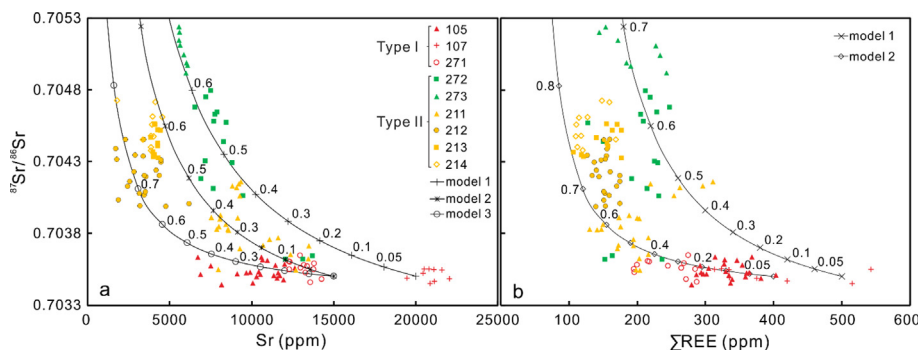
Fig. 9. $^{87}Sr/^{86}Sr$ ratios of calcite in the Miaoya carbonatites. (a) $^{87}Sr/^{86}Sr$ vs. Sr concentration (ppm). Binary mixing model curves between the fluids with syenite assimilation and primary calcite. The $^{87}Sr/^{86}Sr$ ratio is assumed to be 0.727 in the fluids and 0.7035 in the primary calcite in the model. Sr content of the fluids is taken to be 100 ppm, 300 ppm and 500 ppm in models 1, 2, and 3, and Sr content of 20000 ppm is adopted in model 1 and 15000 ppm in models 2 and 3 for primary calcite. (b) $^{87}Sr/^{86}Sr$ vs. REE (ppm). Mixing model curves are characterized by the same Sr isotope ratio in a, the REE abundances of 400 ppm and 500 ppm are adopted for primary calcite, whereas 50 ppm and 100 ppm are used for hydrothermal fluids in models 1 and 2, respectively. Tick marks represent the fraction of hydrothermal fluid mixed with primary calcite.

define a large variation range from 0.70346 to 0.70524 (Fig. 9). The extremely coarse-grained calcite from a Type II carbonatite sample (MY273; Fig. 3a) is characterized by the most radiogenic Sr isotopic compositions with an average $^{87}Sr/^{86}Sr$ value of 0.70508; moreover, a coarse-grained calcite crystal displays a progressive, increasing trend for the Sr isotope ratios (0.70492 to 0.70515) from its core towards the rim (analyses MY273-1 to MY273-4 in SM Table 4). For calcite located within the carbonatite lens in contact with the syenite (Fig. 1d), increasing $^{87}Sr/^{86}Sr$ ratios are observed from the center (0.70354–0.70416; Sample MY211) to the edge (0.70438–0.70473; Sample MY214; Fig. 9). In addition, the fine-grained calcite displays more radiogenic Sr isotopic compositions compared to the adjacent coarse-grained calcite within the Type II carbonatite (Sample MY211; Fig. 7). In general, the variable Sr isotope ratios recorded in calcite show negative correlations with both Sr and REE contents (Fig. 9). The very fine-grained ankerite matrix containing tiny REE-minerals within the ferrocarbonatite veins is characterized by consistently higher $^{87}Sr/^{86}Sr$ isotopic compositions with an average value of 0.70427 (SM Table 4).

5.5. C-O isotopic compositions of calcite separates

The C and O isotopic compositions of calcite separates from the Miaoya carbonatite are variable with $\delta^{13}C_{VPDB}$ values ranging from −6.8 to −3.3 ‰ and $\delta^{18}O_{VSMOW}$ values that range from 8.5 to 12.0 ‰ (SM Table 5). These intervals overlap with previously reported C and O isotope data for Miaoya carbonatites (Fig. 10; Xu et al., 2014; Çimen et al., 2018; Su et al., 2019; Zhang et al., 2019a). Most of the C and O isotope data plot outside and to the right of the primary igneous carbonate (PIC) box with only three Type I carbonatite samples plotting within the box (Fig. 10; Taylor et al., 1967; Keller and Hoefs, 1995).

Calcite has been further characterized by in situ C isotopic measurements using LA-MC-ICP-MS. These compositions in general overlap the bulk (whole rock) analyses,

but do define a wider range of $\delta^{13}C$ values, ranging from −7.1 to −2.2 ‰, in comparison to the latter (Fig. 11a, b; SM Tables 5 and 6). The $\delta^{13}C$ values of calcite in Type I carbonatite range from −7.1 to −4.2 ‰, whereas calcite in Type II carbonatite is characterized by a greater variation (−7.0 to −2.2 ‰; Fig. 11a, b).

6. DISCUSSION

6.1. Geochemical discrimination of primary versus metasomatic calcite

Carbonatite melts are characterized by both lower viscosity and density compared to their silica-rich counterparts, which ensures their rapid ascent from the mantle to shallow crustal levels (e.g., Dobson et al., 1996). Consequently, a main petrographic feature of primary carbonatite is its typical cumulate texture (Mitchell, 2005), whereas recrystallized carbonatites are commonly mistaken to show igneous textures (Chakhmouradian et al., 2016a). Thus, the dominant carbonate in carbonatite is difficult to identify as either magmatic or recrystallized based solely on petrographic evidences (Figs. 2 and 3). Recent studies have demonstrated that the trace element compositions of magmatic carbonates can be adopted for deciphering the petrogenetic history, and mineral chemistry also holds insightful evidence in relation to the polygenetic history of carbonatites (Chakhmouradian et al., 2016b; Ranta et al., 2018; Chen et al., 2020). Chondrite normalized REE patterns of calcite have been shown to serve as good indicators of formational environments (Chakhmouradian et al., 2016b). For example, magmatic calcite typically shows negatively sloping REE patterns with $(La/Yb)_N$ in the range of 4 to 200, whereas hydrothermal calcite is characterized by either higher or lower $(La/Yb)_N$ ratios (Chakhmouradian et al., 2016b; Ranta et al., 2018). Given the large range of trace element ratios defined by magmatic calcite, their corresponding isotopic compositions serve as more important forensic signatures for magmatic vs. meta-
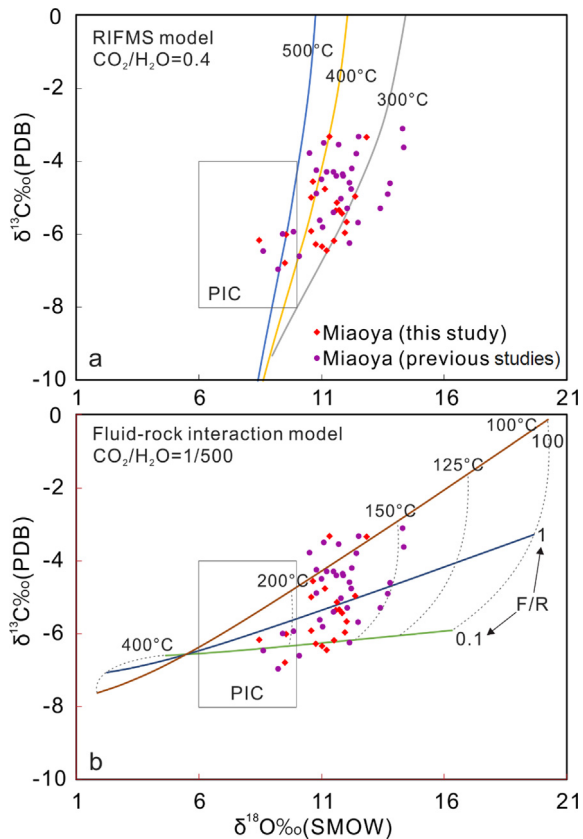
Fig. 10. $\delta^{13}C$ vs. $\delta^{18}O$ plots display the C and O isotope data for calcite from the Miaoya carbonatite complex. The lines in (a) Rayleigh isotopic fractionation from a multi-component source (RIFMS) represent the trend in isotopic composition of calcite shown with the closed-system Rayleigh-type fractionation of the carbonatite with its exsolved fluid at 500 °C, 400 °C and 300 °C. The fluid was assumed to have an initial molar CO_2/H_2O ratio of 0.4 and source $\delta^{13}C$ and $\delta^{18}O$ values are −6.5‰ and 9.5‰, respectively. (b) Evolution of the isotopic composition of calcite with initial $\delta^{13}C$ and $\delta^{18}O$ of −6.5‰ and 9.5‰, which interacts with H_2O-CO_2-fluids (CO_2/H_2O = 1/500) with $\delta^{13}C$ and $\delta^{18}O$ of −4‰ and 0‰ in the fluid-rock isotope exchange model (Santos and Clayton, 1995). The fluid-rock ratio varies from 0.1 to 100, and temperature varies from 100 to 400 °C. The fractionation factors were determined using the thermodynamic data of Richet et al. (1977) and Chacko et al. (1991). The field of primary carbonate (PIC) from Taylor et al. (1967) is shown, together with previously reported stable isotope data for Miaoya (Xu et al., 2014; Çimen et al., 2018; Su et al., 2019; Zhang et al., 2019a).

somatic discrimination. Therefore, in situ trace element abundances combined with their corresponding isotopic compositions of calcite will provide additional insights into distinguishing between geochemical signatures for primary calcite from the one that has experienced metasomatic overprinting, such as for the Type II carbonatite samples from Miaoya.

Calcite samples from Type I and Type II carbonatites differ from each other in chemical compositions. Those for equigranular carbonatite (Type I) display the most LREE-enriched chondrite normalized REE patterns with $(La/Yb)_N$ values of 2.1–5.2 (Fig. 5a). This LREE-enrichment is within the lower part of the range defined by worldwide occurrences of magmatic calcite (Chen and Simonetti, 2013; Chakhmouradian et al., 2016b). Nevertheless, this calcite is characterized by near-chondritic Y/Ho ratios similar to those of the silicate rocks formed via CHarge-and-RAdius-Controlled (CHARAC) processes (Bau, 1996; Fig. 5c). Moreover, calcite from Type I carbonatite contains the most pristine isotopic signatures as indicated by their less enriched Sr isotopic compositions and C and O isotopic compositions consistent with a mantle origin (Figs. 9–11). Thus, the combined trace-element and isotopic signatures of calcite in Type I carbonatite suggest that it crystallized from a mantle-derived source. Of note, the equigranular Type I calcite carbonatite (Fig. 2) is similar to the mosaic polygonal texture displayed by the Lackner Lake calcite carbonatite, which is most probably statically recrystallized (Chakhmouradian et al., 2016a). Nevertheless, calcite in Type I carbonatite represents the most pristine trace-element and isotopic signatures in relation to the magmatic calcite, and it is the best representative of primary calcite in the Miaoya carbonatite complex.

Calcite in Type II carbonatite contains lower Sr and REE abundances, and higher Fe and Mn contents compared to that in Type I carbonatite (SM Table 1). The latter is characterized by variable LREE enrichments and a majority show LREE-depleted patterns with the average $(La/Yb)_N$ and $(La/Sm)_N$ < 1 (Fig. 5a, c). The LREE-depleted chondrite normalized patterns have been observed for recrystallized calcite in metasomatic and hydrothermal parageneses (Chakhmouradian et al., 2016b; Ranta et al., 2018). The variable Y/Ho ratios of calcite in Type II carbonatite are higher compared to those of calcite in Type I, and deviate from the chondritic value (Bau, 1996). Of note, calcite from the center (Sample MY211) to the edge (Sample MY 214) of the carbonatite lens is characterized by increasing Y/Ho ratios (Figs. 1 and 5). The associated Sr isotopic compositions of calcite in Type II carbonatite also show variable and definitely more radiogenic signatures compared to the primary calcite in Type I carbonatite (Fig. 9). This feature further supports the notion that the former variety represents a recrystallized phase formed in an open system involving more than one component (e.g., magmatic calcite and hydrothermal fluids). The hydrothermal activity at Miaoya involved fluorine-rich fluids as evidenced by the crystallization of fluorocarbonates as major REE minerals in the Type II carbonatite (Fig. 4). Decoupling between Y and Ho observed in calcite from this paragenesis may be attributed to the differing fluoride complexation of Y and Ho in hydrothermal fluids (Bau, 1996; Migdisov et al., 2009). In addition, the texture of the inequigranular Type II calcite carbonatite is similar to the "core-and-mantle" structures that are common in dynamically recrystallized carbonate rocks (Chakhmouradian et al., 2016a). Thus, the trace-element and isotopic compositions of calcite from the Type II carbonatite may be explained by fluid-assisted recrystallization during late-stage metasomatic activity.
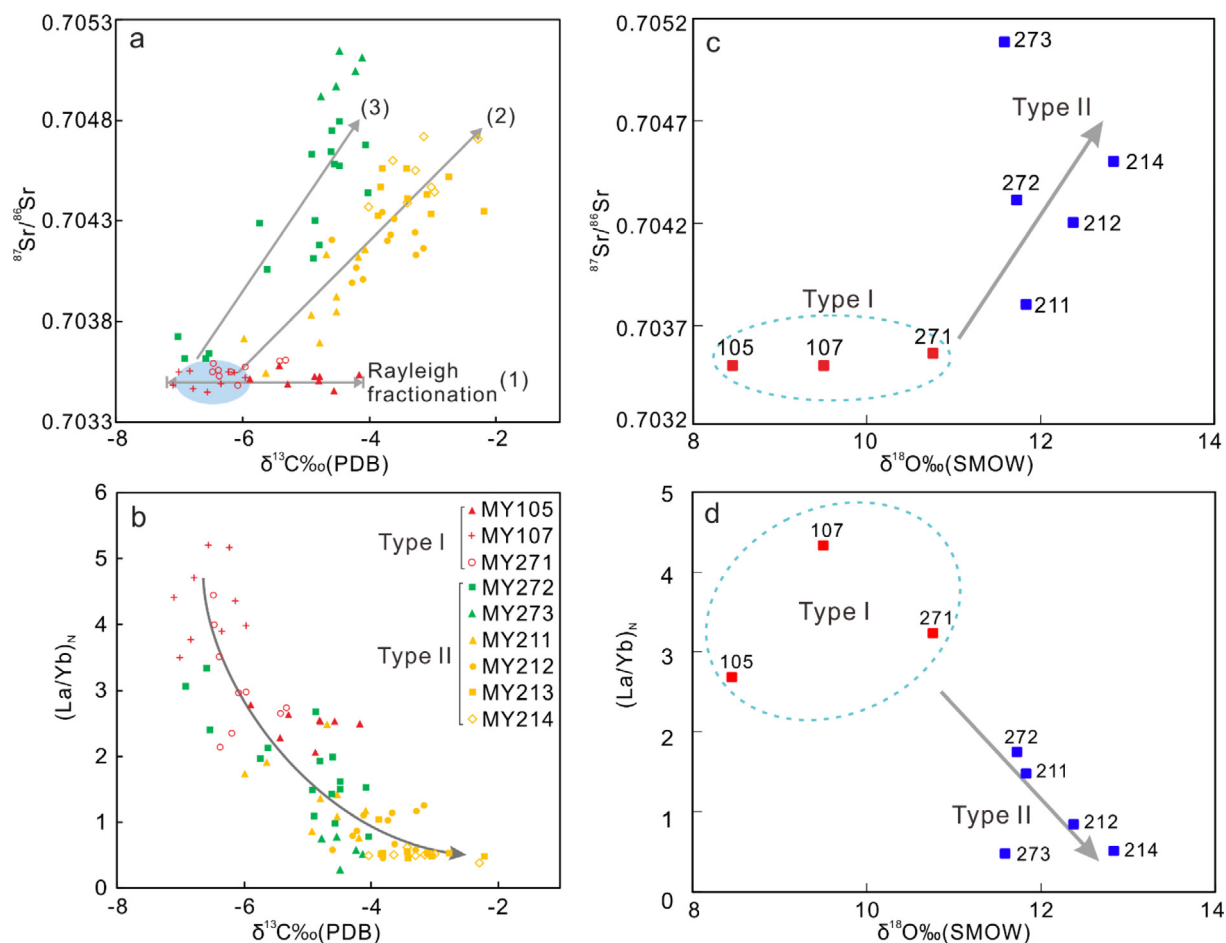
Fig. 11. (a) Three trends identified in the diagram of in situ C isotope composition *vs.* $^{87}Sr/^{86}Sr$ ratios of calcite. (b) Increasing $\delta^{13}C$ values with decreasing $(La/Yb)_N$ values of calcite from Type I to Type II carbonatite. (c and d) Increasing $\delta^{18}O$ values with increasing $^{87}Sr/^{86}Sr$ ratios and decreasing $(La/Yb)_N$ ratios of calcite from Type I to Type II carbonatite.

6.2. Source and evolution of hydrothermal fluids during late-stage metasomatism

The carbon and oxygen isotope data for calcite from the Miaoya carbonatite complex exhibit a large variation with a majority of the Type II carbonatite samples plotting to the right of the primary igneous carbonate field. This feature may be a result of Rayleigh crystal fractionation (i.e., a closed-system carbonate magma/fluid evolution with cooling and crystallization; e.g., Deines, 1989), assimilation of sedimentary carbonate, or addition of external fluids (Santos and Clayton, 1995; Ray and Ramesh, 2000). Given that the Miaoya carbonatite complex was emplaced within the metamorphic silicate rocks along the South Qinling orogenic belt, then Rayleigh-type fractionation or fluid-rock isotope exchange with meteoric water appear to be a more likely processes in producing the observed isotopic variability. Results from both the Rayleigh fractionation and fluid-rock isotope exchange models are shown in Fig. 10. The variable carbon and oxygen isotopic compositions recorded in calcite may be explained by either Rayleigh crystal fractionation giving rise to fluid exsolution from carbonatite in the temperature range of 300–500 °C, and/or interaction of

carbonatite with meteoric water at relatively low temperatures (150–200 °C) (Fig. 10). A previous study suggests that the homogenization temperatures for fluid inclusions in calcite and quartz in the Miaoya carbonatites are in the range of 300–400 °C (Wu et al., 2011). Rayleigh-type fractionation possibly played the dominant role in the generation of variable C and O isotopic compositions recorded in the Miaoya calcite, with the assumption that the calcite is hydrothermal and the homogenization temperatures are close to tapping temperatures. The carbonatite-exsolved fluids precipitated both the late-stage calcite with higher C and O isotopic values (Fig. 10a) and REE minerals at a temperature approximately 300–400 °C.

Metasomatic calcite in Type II carbonatite at Miaoya is characterized by distinct Sr isotopic compositions compared to the primary calcite in Type I carbonatite (Fig. 9). It is somewhat difficult to perturb the original Sr isotopic composition of magmatic calcite with a crust-derived fluid characterized by much lower Sr contents. Here, the more radiogenic Sr isotopic compositions recorded in the metasomatic calcite probably originated from Rb-rich (or high Rb/Sr ratios) minerals, such as feldspar and biotite in the associated syenite (Xu et al., 2015).

K-feldspar is the dominant phase in the associated syenite at Miaoya with high Rb/Sr ratios (21 on average; Xu et al., 2015), which generated abundant radiogenic Sr after its early Paleozoic crystallization with $^{87}Sr/^{86}Sr$ ratios increasing to ∼0.727 until the Triassic (SM Table 4). As shown in Fig. 9, the majority of the variable Sr isotopic and trace element compositions for the metasomatic calcite can be reproduced using a binary mixing model involving carbonatite-exsolved fluids (having experienced syenite assimilation) and primary calcite as the two end-members. Of note, the metasomatic calcite with distinct isotopic and chemical signatures represents variable degrees of interaction between fluids and primary calcite (Fig. 9).

In situ C and Sr isotopic compositions of calcite in Types I and II carbonatites define different trends, as shown in Fig. 11. Calcite in Type I carbonatite defines essentially a horizontal trend (labeled 1). Several Type I calcite grains with restricted carbon isotopic compositions (−6 to −7‰) may be the result of Rayleigh crystal fractionation with a minor amount of solely carbonatite-exsolved fluids without contamination of the syenite during late-stage metasomatism (Fig. 10a). Carbon isotopic values of calcite in Type II carbonatite generally show positive correlations with Sr isotopic values (Trends 2 and 3 in Fig. 11a). The combined Sr-C isotopic variations of calcite in Type II carbonatite most probably result from its interaction with carbonatite-exsolved fluids and syenite assimilation (Figs. 9–11). The two different trends (2 and 3) observed for calcite in Type II carbonatite may represent variations in composition and/or temperature of the hydrothermal fluids coupled with varying degrees of recrystallization (Fig. 11a). Similarly, the O isotopic compositions of calcite from the Type I carbonatite show limited variation and are consistent with the range of primary carbonate (Keller and Hoefs, 1995); whereas Type II carbonatite is characterized by higher oxygen isotopic values that correlate positively with $^{87}Sr/^{86}Sr$ ratios (Fig. 11a, c). Metasomatic calcite with the highest C and O isotopic values represent those formed from fluids with the most radiogenic Sr isotopic ratios inherited from syenite (Figs. 10 and 11).

Thus, the various models based on the combined trace-element and isotopic compositions of calcite in the Miaoya carbonatites indicate that late-stage metasomatism may explain the petrographic, mineralogical, and chemical variations observed in the Miaoya carbonatites. The metasomatism involved hydrothermal fluids that were mainly derived from carbonatite with or without syenite assimilation; the late-stage fluids that experienced syenite assimilation yielded Type II carbonatite characterized by inequigranular calcite and represents the most intense metasomatism. Type I carbonatite composed of equigranular calcite represents the carbonatite least affected by metasomatic overprint, presumably involving only internal carbonatite-exsolved fluids (if any).

6.3. Mobilization and redeposition of REEs during late-stage metasomatism

Previous investigations have shown that secondary REE minerals can form during late-stage hydrothermal processes, in which REEs are mobilized from the primary magmatic carbonate and/or apatite to precipitate monazite and fluorocarbonate (Downes et al., 2014; Li and Zhou, 2015). Mobilization of REEs in hydrothermal systems has been widely accepted based on evidence from both experimental work and natural samples (Sheard et al., 2012; Gysi and Williams-Jones, 2013; Li and Zhou, 2015). On the basis of combined petrological, mineralogical and geochemical evidence, we propose two important mechanisms for the development of REE mineralization at Miaoya: (1) dissolution-reprecipitation of fluorapatite with monazite mineralization, and (2) dissolution-reprecipitation of calcite with monazite and fluorocarbonate mineralization.

Dissolution-reprecipitation is a fluid-mineral reaction where the mineral is replaced with an entirely new phase, or the same phase with a different composition to reduce the free energy of a system (Downes et al., 2014; Broom-Fendley et al., 2016). Dissolution-reprecipitation of apatite has been shown as an important mechanism in REE mineralization (monazite and xenotime) in magmatic-hydrothermal systems from a variety of deposits including iron-oxide-apatite (Harlov et al., 2016; Palma et al., 2019), carbonatite-related (Broom-Fendley et al., 2016; Chakhmouradian et al., 2017; Giebel et al., 2017), Fe-Cu-(REE) (Li and Zhou, 2015), and REE-phosphate types (Andersson et al., 2019), and in a variety of other rock types including granulite-facies metapelites (Harlov et al., 2007), nepheline clinopyroxenites (Krause et al., 2013), and granitic pegmatite (Alves et al., 2019). Monazite inclusions within apatite and/or deposited on apatite crystal rims exhibit characteristic dissolution-reprecipitation textures (Fig. 2; Broom-Fendley et al., 2016; Alves et al., 2019; Andersson et al., 2019). Apatite dissolution and monazite-apatite precipitation reactions are coupled because the rates of dissolution and reprecipitation must be similar if not equal driven by a minimization in Gibbs free energy (Krause et al., 2013). For most REE mineralization (e.g., monazite and xenotime) formation events, the required REE availability may be supplied by dissolution-reprecipitation of apatite; thus, an external REE source is not required. REE-enriched fluids were invoked for the precipitation of post-magmatic monazite via the dissolution of apatite from the Phalaborwa complex (Giebel et al., 2017).

At Miaoya, monazite crystallization along fluorapatite rims has been identified in both types of carbonatites. The fluorapatite zones adjacent to monazite are characterized by relative LREE-depletion (Fig. 5b). Thus, it is certain that at least a portion of the monazite grains formed directly from the associated fluorapatite. The fluorapatite is characterized by relatively constant $^{87}Sr/^{86}Sr$ ratios and yields an average value of 0.70359 compared to the variable Sr isotopic compositions of the associated calcite. Creaser and Gray (1992) demonstrated that initial $^{87}Sr/^{86}Sr$ ratios of apatite can be preserved and are not modified as a result of low temperature (<300 °C) hydrothermal alteration or magmatic cooling. They suggest that diffusional modification of $^{87}Sr/^{86}Sr$ in fluorapatite would only affect the rims of many crystals during low-temperature metamorphism and hydrothermal alteration. The relatively constant Sr isotopic compositions of the fluorapatite suggest that either

this mineral is more resistant to fluid-mineral reaction during late-stage metasomatism (under certain conditions), or possibly difficult to be contaminated by the fluids due to its high Sr contents (on average, 9922 ppm; SM Table 2).

Carbonate is the dominant mineral phase in carbonatites with the capacity to host REEs, and its role in REE mineralization within magmatic-hydrothermal systems may have thus far been underestimated. The chemical composition of calcite is easily affected by metasomatic fluids over a wide range of temperatures, and generally the solubility of calcite increases with decreasing temperature (Fein and Walther, 1987; Ray and Ramesh, 2000; Ranta et al., 2018). The availability of REEs for incorporation into recrystallized calcite is mostly controlled by fluid-mineral partitioning due to growth competition between co-precipitating phases, which are affected by the transient gradient in P, T, fO$_2$, and fCO$_2$ of the hydrothermal fluids (Migdisov et al., 2016). Experimental works have demonstrated that F$^-$, Cl$^-$, OH$^-$, CO$_3^{2-}$, SO$_4^{2-}$, and PO$_4^{3-}$ anions are effective REE complexing ligands in solution (Sheard et al., 2012; Migdisov et al., 2009, 2016), and LREE-chloride and -fluoride complexes are more stable compared to their HREE counterparts (Migdisov et al., 2016). At Miaoya, the metasomatic calcite with highest C, O, and Sr isotopic values is also characterized by the most depleted REE contents and lowest (La/Yb)$_N$ ratios (Fig. 11b, d). The sequential changes of REE distribution from primary to metasomatic calcite may be attributed to the variable stability of different REEs in hydrothermal fluids and/or the co-precipitation of REE minerals, such as monazite and fluorocarbonates (Figs. 9 and 11). The preferential mobility of LREEs led to their release from the primary calcite, and the subsequently generated LREE-enriched fluids that eventually deposited the secondary monazite and fluorocarbonate were then disseminated in carbonatite or within veins (Figs. 2–4). Fluid-assisted recrystallization of LREE-depleted calcite associated with LREE mineralization played a significant role in the formation of the Miaoya REE deposit. This type of dissolution-reprecipitation mechanism of calcite has been reported from other carbonatite complexes as well, including Bear Lodge (USA, Moore et al., 2015; Andersen et al., 2017), Aley (Canada, Chakhmouradian et al., 2015; 2016b), and Grønnedal–Íka (Greenland, Ranta et al., 2018). In addition, LREE-depleted carbonate has also been reported in other REE deposits such as Bayan Obo (China, Chen et al., 2020), Bachu (China, Cheng et al., 2018), and Haast River (New Zealand, Cooper et al., 2015). Metasomatic reworking that occurred at these complexes may share similar formational mechanisms that involved derivation of carbonatitic fluids, followed by reaction and redeposition.

The modal distribution of calcite and fluorapatite in the Miaoya carbonatite samples varies from 80-100 vol.% and 0–20 vol.%, respectively. Assuming a carbonatite sample composed of 100 vol.% calcite, LREEs released through the metasomatic process will result in the formation of 0.07 vol.% monazite (or fluorocarbonate) with the estimated LREE contents of 424 and 38 ppm for primary and metasomatic calcite, respectively (SM Table 1). Assuming the average 10 vol.% modal distribution of fluorapatite,

LREEs released from fluorapatite will form 0.16 vol.% monazite using LREE contents of the most enriched and depleted apatite (9794 and 997 ppm, respectively; SM Table 2). For a sample with 90 vol.% of calcite and 10 vol.% of apatite, approximately 0.22 vol.% monazite or fluorocarbonate can be generated with the LREEs released from metasomatic calcite and fluorapatite (SM Tables 1 and 2). Based on the LREE contents reported for calcite, apatite and associated bulk rock, the modal distribution of monazite/fluorocarbonate is estimated to vary from 0.06 vol.% to 0.24 vol.% with an average value of 0.18 vol.% for the investigated carbonatite samples (Xu et al., 2010). Thus, the precipitated amount of REE minerals through calcite and apatite metasomatism match the high end of the observed monazite distribution range in the carbonatite samples reported in Xu et al. (2010). Of note, the distribution of REE minerals in the Miaoya carbonatite samples is highly variable (Xu et al., 2010, 2015; Su et al., 2019), and it is difficult to predict the distribution of REEs among different mineral phases without conducting a detailed field and geochemical exploration of the complex. However, based on the mass balance calculations, the REEs released from the metasomatic carbonate and fluorapatite show great potential to serve as the major source for the formation of secondary REE minerals. As described earlier, almost all monazite and bastnäsite in both carbonatite and syenite are reported with a Triassic age of approximately 210–230 Ma, with the exception of two monazite crystals from carbonatite characterized by a U-Pb age of 414 ± 11 Ma (Xu et al., 2014; Ying et al., 2017; Zhang et al., 2019b). In summary, the REE mineralization at Miaoya is formed predominantly during the Triassic due to dissolution-reprecipitation of calcite and fluorapatite, with a small quantity of monazite that probably crystallized during the Paleozoic magmatism.

The processes and sequence of magmatic and metasomatic events leading to the REE mineralization at Miaoya is summarized in Fig. 12. During the early Paleozoic magmatism at Miaoya, the REEs were preferentially incorporated into fluorapatite and calcite (Fig. 12a). The presence of small-scale faults and shear zones provided a preferred pathway for the Triassic-aged metasomatic activity (Fig. 12b). Fluids emanated from carbonatite (with or without syenite assimilation) and mobilized the LREEs from calcite and fluorapatite, and these LREE-enriched fluids in turn formed REE minerals in the carbonatite, or within micro-veins, vugs, and fractures located within carbonatites and syenites.

6.4. Implications for metasomatism associated REE mineralization in carbonatites

In a global context, REE mineralization in carbonatite-related large REE deposits formed by purely igneous processes is rare (Smith et al., 2016). It is now accepted that carbonatite-associated REE deposits were subjected to multiple stages of hydrothermal overprinting and/or metamorphism (Downes et al., 2016; Song et al., 2018). In the case of Miaoya, the metasomatism took place during the Triassic, which is totally independent of the early Paleozoic carbon-
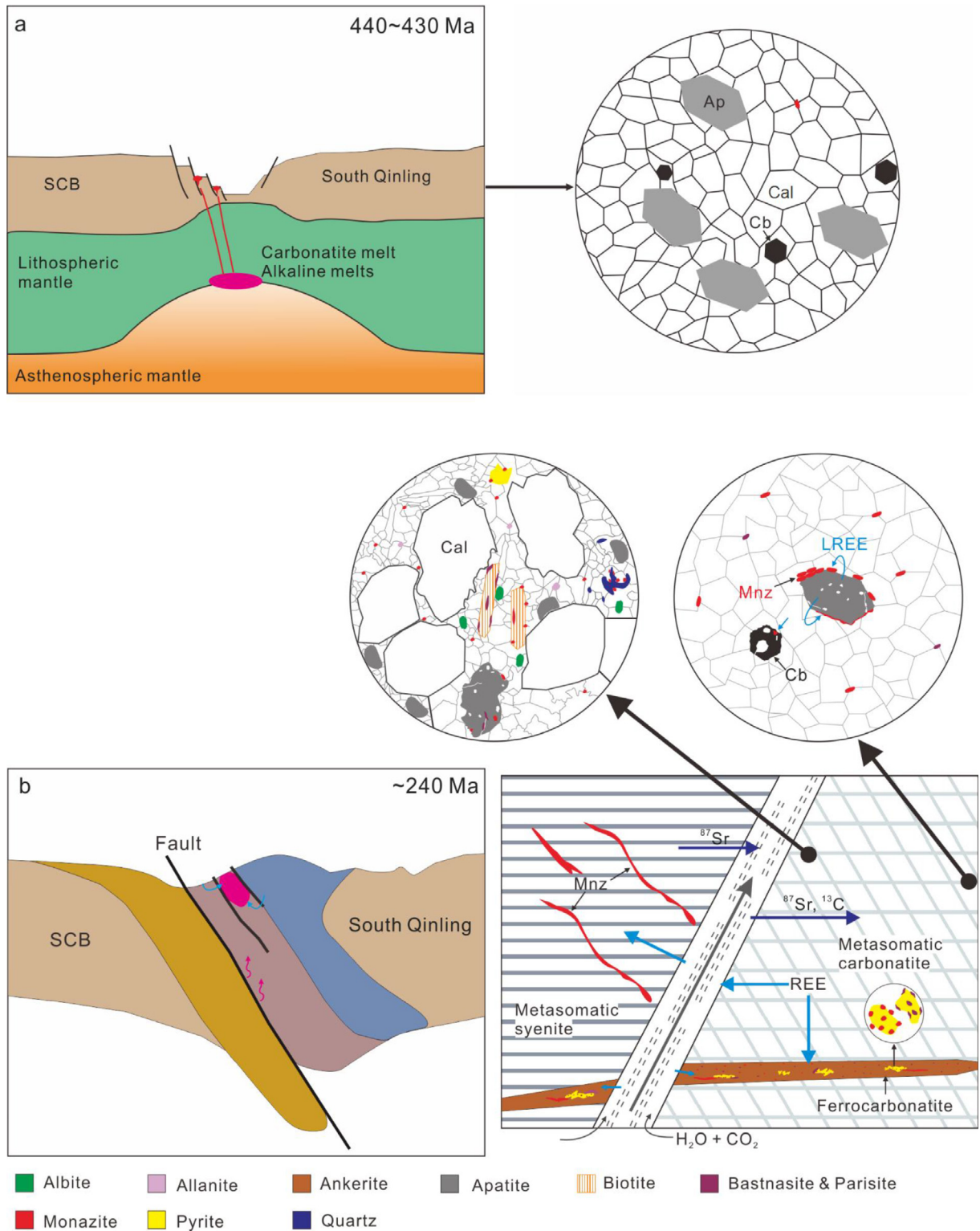
Fig. 12. A cartoon illustrating the genetic model and REE mineralization processes for the Miaoya complex.

atite magmatic event (Xu et al., 2014; Zhu et al., 2016; Ying et al., 2017; Zhang et al., 2019b; Su et al., 2019). Similar late-stage, independent metasomatic overprinting is reported in other REE deposits, and can be protracted over

hundreds of millions of years (e.g., Downes et al., 2016; Slezak and Spandler, 2019). For example, it has been argued that the Bayan Obo REE deposits formed as a result of Mesoproterozoic carbonatite emplacement with signifi-

cant Paleozoic metasomatic reworking based on a variety of isotopic age results for various minerals and bulk rocks (Smith et al., 2000; Ling et al., 2013; Yang et al., 2017; Yang et al., 2019; Chen et al., 2020 and references therein). In another example, the U-Pb dates for zircon define a definitive magmatic age of 1370 Ma for the Gifford Creek carbonatite complex (Australia), whereas the much younger ages for the associated monazite and apatite (1300–815 Ma) represent the timing of the tectonically induced hydrothermal activity (Pirajno et al., 2014; Zi et al., 2017; Slezak and Spandler, 2019). At the Cummins Range, carbonatite emplacement occurred at ~1.0 Ga, whereas the hydrothermal monazite is characterized by ages ranging from 900 - 590 Ma, which clearly reflect a prolonged history of hydrothermal alteration (Downes et al., 2014, 2016). In other carbonatite-alkaline complexes, the late-stage hydrothermal process(es) may have occurred as a continuous evolution from the magmatism. For example, the Bear Lodge REE deposits are the result of continuous evolution through magmatic, carbo-hydrothermal, late hydrothermal, and supergene weathering stages (Andersen et al., 2017). The evolution of the 2060 Ma old Phalaborwa carbonatite complex also involved continuous development from orthomagmatic to late-magmatic stages and postmagmatic overprint (Giebel et al., 2017).

In the formation of REE-enriched carbonatites, the preferred argument has been that carbonate magmas originate from REE-re-fertilized mantle sources, which are subsequently emplaced into the overlying crust, and then exsolve REE-rich fluids that lead to the formation of REE deposits (Xie et al., 2009; Smith et al., 2016). The latter happens in two situations: (1) the carbonatitic magma ascends through favorable pathways where REE-rich fluids exsolve from the cooling magma (Hou et al., 2015); and (2) the emplaced carbonatites are reactivated with carbonatite-exsolved REE-rich fluids during the late-stage metasomatism (Downes et al., 2016; Trofanenko et al., 2016; Giebel et al., 2017). The Mianning-Dechang deposits located along the west margin of the Yangtze Craton are an example where the magma exsolved oxidized, REE-rich fluids during stress relaxation as they ascended along trans-lithospheric faults (Xie et al., 2009; Hou et al., 2015). The latter study proposed that REE-rich fluids originated from melting of the subcontinental lithospheric mantle that was previously metasomatized by high-flux REE- and CO_2-rich fluids derived from subducted marine sediments. Furthermore, it was suggested that cratonic margins or orogenic belts represent more fertile tectonic settings as these may have initially been affected by subduction-related processes in accretionary orogens that potentially fertilize the overlying lithospheric mantle (Hou et al., 2015; Moore et al., 2015; Xue et al., 2018, 2020; Zheng et al., 2019). Moreover, late-stage tectono-thermal events at these tectonic settings can refertilize volatile-rich rocks (e.g., carbonatites) via metasomatic activity. This process will result in the production of carbonatite exsolved fluids, which remobilize and redeposit REEs from the original REE-bearing minerals (calcite, apatite) to form late-stage REE-bearing minerals. This is our preferred petrogenetic model for production of the Miaoya REE deposit, which has direct implications for other worldwide REE deposits

such as Bayan Obo, Cummins Range, Bear Lodge, and Phalaborwa (Downes et al., 2014; Trofanenko et al., 2016; Andersen et al., 2017; Giebel et al., 2017; Chen et al., 2020). The role of late-stage metasomatism in REE mineralization for giant REE deposits may have been underestimated to date due to the complex overprinting of both petrographic and geochemical signatures (Smith et al., 2016; Song et al., 2018; Chen et al., 2020). Furthermore, regional, large-scale faults and fractures related to the active tectonism are common in cratonic edges and orogenic belts, which provide channels and pathways for circulation of hydrothermal fluids (Fig. 12). Therefore, we suggest that carbonatites located in these tectonic settings possess great potential for hosting economic REE deposits.

7. CONCLUSIONS

Calcite in two textural types of carbonatite from Miaoya shows distinct Sr-C-O isotopic and trace-element signatures, whereas fluorapatite in the two rock types display similar trace-element abundances and consistent Sr isotope compositions. The observed textural and geochemical variations in calcite and fluorapatite at the Miaoya complex suggest interaction with carbonatite-exsolved fluids associated with Triassic metasomatism. The late-stage metasomatic reworking at the Miaoya REE deposit is an example of repreciprecipitating REEs from primary minerals (calcite and fluorapatite) as secondary REE minerals (monazite and fluorocarbonates) through dissolution-repreciprecipitation mechanisms. The process of metasomatism may be underestimated in the formation of giant REE deposits, and its role in generating petrographic, chemical, and isotopic complexities should be taken into consideration when deciphering the petrogenetic history of the other carbonatite-related REE deposits.

Declaration of Competing Interest

The authors declare that they have no known competing financial interests or personal relationships that could have appeared to influence the work reported in this paper.

APPENDIX A. SUPPLEMENTARY MATERIAL

Supplementary data to this article can be found online at https://doi.org/10.1016/j.gca.2020.04.028.

REFERENCES

Alves F. E. A., Neumann R., Avila C. A. and Faulstich F. R. L. (2019) Monazite-(Ce) and xenotime-(Y) microinclusions in fluorapatite of the pegmatites from the Volta Grande mine, minas Gerais state, southeast Brazil, as witnesses of the dissolution-reprecipitation process. *Mineral. Mag.* **83**, 595–606.

Andersen A. K., Clark J. G., Larson P. B. and Donovan J. J. (2017) REE fractionation, mineral speciation, and supergene enrichment of the Bear Lodge carbonatites, Wyoming, USA. *Ore Geol. Rev.* **89**, 780–807.

Andersson S. S., Wagner T., Jonsson E., Fusswinkel T. and Whitehouse M. J. (2019) Apatite as a tracer of the source, chemistry and evolution of ore-forming fluids: The case of the Olserum-Djupedal REE-phosphate mineralization, SE Sweden. *Geochim. Cosmochim. Acta* **225**, 163–187.

Bau M. (1996) Controls on the fractionation of isovalent trace elements in magmatic and aqueous systems: evidence from Y/Ho, Zr/Hf, and lanthanide tetrad effect. *Contrib. Mineral. Petrol.* **123**, 323–333.

Broom-Fendley S., Styles M. T., Appleton J. D., Gunn G. and Wall F. (2016) Evidence for dissolution-reprecipitation of apatite and preferential LREE mobility in carbonatite-derived late-stage hydrothermal processes. *Am. Mineral.* **101**, 596–611.

Chacko T., Mayeda T. K., Clayton R. N. and Goldsmith J. R. (1991) Oxygen and carbon isotope fractionation between CO_2 and calcite. *Geochim. Cosmochim. Acta* **55**, 2867–2882.

Chakhmouradian A. R., Reguir E. P., Kressall R. D., Crozier J., Pisiak L. K., Sidhu R. and Yang P. (2015) Carbonatite-hosted niobium deposit at Aley, northern British Columbia (Canada): Mineralogy, geochemistry and petrogenesis. *Ore Geol. Rev.* **64**, 642–666.

Chakhmouradian A. R., Reguir E. P. and Zaitsev A. N. (2016a) Calcite and dolomite in intrusive carbonatites. I. Textural variations. *Miner. Petrol.* **110**, 333–360.

Chakhmouradian A. R., Reguir E. P., Couëslan C. and Yang P. (2016b) Calcite and dolomite in intrusive carbonatites. II. Trace-element variations. *Miner. Petrol.* **110**, 361–377.

Chakhmouradian A. R., Reguir E. P., Zaitsev A. N., Couëslan C., Xu C., Kynicky J., Mumin A. H. and Yang P. (2017) Apatite in carbonatitic rocks: Compositional variation, zoning, element partitioning and petrogenetic significance. *Lithos* **275**, 188–213.

Chen L., Liu Y. S., Hu Z. C., Gao S., Zong K. Q. and Chen H. H. (2011) Accurate determinations of fifty-four major and trace elements in carbonate by LA-ICP-MS using normalization strategy of bulk components as 100%. *Chem. Geol.* **284**, 283–295.

Chen W. and Simonetti A. (2013) In-situ determination of major and trace elements in calcite and apatite, and U-Pb ages of apatite from the Oka carbonatite complex: Insights into a complex crystallization history. *Chem. Geol.* **353**, 151–172.

Chen W., Liu H. Y., Lu J., Jiang S. Y., Simonetti A., Xu C. and Zhang W. (2020) The formation of the ore-bearing dolomite marble from the giant Bayan Obo REE-Nb-Fe deposit, Innder Mongolia: insights from micron-scale geochemical data. *Miner. Deposita* **55**, 131–146.

Chen W., Lu J., Jiang S. Y., Ying Y. C. and Liu Y. S. (2018) Radiogenic Pb reservoir contributes to the rare earth element (REE) enrichment in South Qinling carbonatites. *Chem. Geol.* **494**, 80–95.

Chen W., Lu J., Jiang S. Y., Zhao K. D. and Duan D. F. (2017) In situ carbon isotope analysis by laser ablation MC-ICP-MS. *Anal. Chem.* **89**, 13145–13421.

Cheng Z. G., Zhang Z. C., Aibai A., Kong W. L. and Holtz F. (2018) The role of magmatic and post-magmatic hydrothermal processes on rare-earth element mineralization: A study of the Bachu carbonatites from the Tarim Large Igneous Province, NW China. *Lithos* **314–315**, 71–87.

Çimen O., Kuebler C., Monaco B., Simonetti S. S., Corcoran L., Chen W. and Simonetti A. (2018) Boron, carbon, oxygen and radiogenic isotope investigation of carbonatite from the Miaoya complex, central China: Evidences for late-stage REE hydrothermal event and mantle source heterogeneity. *Lithos* **322**, 225–237.

Cooper A. F., Collins A. K., Palin J. M. and Spratt J. (2015) Mineralogical evolution and REE mobility during crystallization of ancylite-bearing ferrocarbonatite, Haast River, New Zealand. *Lithos* **216–217**, 324–337.

Creaser R. A. and Gray C. M. (1992) Preserved initial $^{87}Sr/^{86}Sr$ in apatite from altered felsic igneous rocks: A case study from the Middle Proterozoic of South Australia. *Geochim. Cosmochim. Acta* **56**, 2789–2795.

Deines P. (1989) Stable isotope variations in carbonatites. In *Carbonatites: Genesis and Evolution* (ed. K. Bell). Unwin Hyman, London, pp. 105–148.

Dobson D. V., Jones A. P., Rabe R., Sekine T., Kurita K., Taniguchi T., Kondo T., Kato T., Shimomura O. and Urakawa S. (1996) In-situ measurement of viscosity and density of carbonate melts at high pressure. *Earth Planet. Sci. Lett.* **143**, 207–215.

Dong Y. P., Zhang G. W., Neubauer F., Liu X. M., Genser J. and Hauzenberger C. (2011) Tectonic evolution of the Qinling orogen, China: review and synthesis. *J. Asian Earth Sci.* **41**, 213–237.

Downes P. J., Demény A., Czuppon G., Jaques A. L., Verrall M., Sweetapple M., Adams D., McNaughton N. J., Gwalani L. G. and Griffin B. J. (2014) Stable H-C-O isotope and trace element geochemistry of the Cummins Range Carbonatite Complex, Kimberley region, Western Australia: implications for hydrothermal REE mineralization, carbonatite evolution and mantle source regions. *Miner. Deposita* **49**, 905–932.

Downes P. J., Dunkley D. J., Fletcher I. R., McNaughton N. J., Rasmussen B., Jaques A. L., Verrall M. and Sweetapple M. T. (2016) Zirconolite, zircon and monazite-(Ce) U-Th-Pb age constraints on the emplacement, deformation and alteration history of the Cummins Range Carbonatite Complex, Halls Creek Orogen, Kimberley region, Western Australia. *Miner. Petrol.* **110**, 199–222.

Fein J. B. and Walther J. V. (1987) Calcite solubility in supercritical CO_2-H_2O fluids. *Geochim. Cosmochim. Acta* **51**, 1665–1673.

Giebel R. J., Gauert C. D. K., Marks M. A. W., Costin G. and Markl G. (2017) Multi-stage formation of REE minerals in the Palabora Carbonatite Complex, South Africa. *Am. Mineral.* **102**, 1218–1233.

Gysi A. P. and Williams-Jones A. E. (2013) Hydrothermal mobilization of pegmatite-hosted REE and Zr at Strange Lake, Canada: A reaction path model. *Geochim. Cosmochim. Acta* **122**, 324–352.

Harlov D. E., Marschall H. R. and Hanel M. (2007) Fluorapatite-monazite relationships in granulite-facies metapelites, Schwarzwald, southwest Germany. *Mineral. Mag.* **71**, 223–234.

Harlov D. E., Meighan C. J., Kerr I. D. and Samson I. M. (2016) Mineralogy, chemistry and fluid-aided evolution of the Pea Ridge Fe oxide-(Y+REE) deposit, Southeast Missouri, USA. *Econ. Geol.* **111**, 1963–1984.

Hou Z. Q., Liu Y., Tian S. H., Yang Z. M. and Xie Y. L. (2015) Formation of carbonatite-related giant rare-earth-element deposits by the recycling of marine sediments. *Sci. Rep.* **5**, 10231. https://doi.org/10.1038/srep10231.

Keller, J., Hoefs, J., 1995. Stable isotope characteristics of recent natrocarbonatite from Oldoinyo Lengai. In: Bell, K., Keller, J. (Eds.), Carbonatite Volcanism: OldoinyoLengai and the Petro-

genesis of Natrocarbonatites: IAVCE I, Proc. Volcanol. 4, pp. 113–123.

Krause J., Harlov D. E., Pushkarev E. V. and Brugmann G. E. (2013) Apatite and clinopyroxene as tracers for metasomatic processes in nepheline clinopyrxoenites of Uralian-Alaskan-type complexes in the Ural Mountains, Russian Federation. *Geochim. Cosmochim. Acta* **121**, 503–521.

Li X. C. and Zhou M. F. (2015) Multiple stages of hydrothermal REE remobilization recorded in fluorapatite in the Paleoproterozoic Yinachang Fe–Cu–(REE) deposit, Southwest China. *Geochim. Cosmochim. Acta* **166**, 53–73.

Ling M. X., Liu Y. L., Williams I. S., Teng F. Z., Yang X. Y., Ding X., Wei G. J., Xie L. H., Deng W. F. and Sun W. D. (2013) Formation of the world's largest REE deposit through protracted fluxing of carbonate by subduction-derived fluids. *Sci. Rep.* **3**, 1776. https://doi.org/10.1038/srep01776.

Ling W. L., Ren B. F., Duan R. C., Liu X. M., Mao X. W., Peng L. H., Liu Z. X., Cheng J. P. and Yang H. M. (2007) Timing of the Wudangshan, Yaolinghe volcanic sequences and mafic sills in South Qinling: U-Pb zircon geochronology and tectonic implication. *Chin. Sci. Bull.* **53**, 2192–2199.

Liu Y. L., Ling M. X., Williams I. S., Yang X. Y., Wang C. Y. and Sun W. D. (2018) The formation of the giant Bayan Obo REE-Nb-Fe deposit, North China, Mesoproterozoic carbonatite and overprinted Plaeozoic dolomitization. *Ore Geol. Rev.* **92**, 73–83.

Liu Y. S., Hu Z. C., Gao S., Gunther D., Xu J., Gao C. G. and Chen H. H. (2008) In situ analysis of major and trace elements of anhydrous minerals by LA-ICP-MS without applying an internal standard. *Chem. Geol.* **257**, 34–43.

Liu S., Fan H. R., Groves D. I., Yang K. F., Yang Z. F. and Wang Q. W. (2020) Multiphase carbonatite-related magmatic and metasomatic processes in the genesis of the ore-hosting dolomite in the giant Bayan Obo REE-Nb-Fe deposit. *Lithos* **354–355**, 105359. https://doi.org/10.1016/j.lithos.2019.105359.

Ludwig K.R., 2003. User's Manual for Isoplot 3.00a Geochronological Toolkit for Microsoft Excel. Berkeley Geochronology Center, Berkeley, CA.

McDonough W. F. and Sun S. S. (1995) The composition of the Earth. *Chem. Geol.* **120**, 223–253.

Migdisov A. A., Williams-Jones A. E. and Wagner T. (2009) An experimental study of the solubility and speciation of the Rare Earth Element (III) in fluoride- and chloride-bearing aqueous solutions at temperatures up to 300°C. *Geochim. Cosmochim. Acta* **73**, 7087–7109.

Migdisov A. A., Williams-Jones A. E., Brugger J. and Caporuscio F. A. (2016) Hydrothermal transport, deposition, and fractionation of the REE: Experimental data and thermodynamic calculations. *Chem. Geol.* **439**, 13–42.

Milani L., Bolhar R., Frei D., Harlov D. E. and Samuel V. O. (2017) Light rare earth element systematics as a tool for investigating the petrogenesis of phoscorite-carbonatite associations, as exemplified by the Phalaborwa Complex, South Africa. *Miner. Deposita* **52**, 1105–1125.

Mitchell R. H. (2005) Carbonatites and carbonatites and carbonatites. *Can. Mineral.* **43**, 2049–2068.

Moore M., Chakhmouradian A. R., Mariano A. N. and Sidhu R. (2015) Evolution of rare-earth mineralization in the Bear Lodge carbonatite, Wyoming: Mineralogical and isotopic evidence. *Ore Geol. Rev.* **64**, 499–521.

Palma G., Barra F., Reich M., Valencia V., Simon A. C., Vervoort J., Leisen M. and Romero R. (2019) Halogens, trace element concentrations, and Sr-Nd isotopes in apatite from iron oxide-apatite (IOA) deposits in the Chilean iron belt: evidence for magmatic and hydrothermal stages of mineralization. *Geochim. Cosmochim. Acta* **246**, 515–540.

Pirajno F., González-Álvarez I., Chen W., Kyser K. T., Simonetti A., Leduc E. and LeGras M. (2014) The Gifford Creek Ferrocarbonatite Complex, Gascoyne Province, Western Australia: associated fenitic alteration and a putative link with the ~1075 Ma Warakurna LIP. *Lithos* **202–203**, 100–119.

Ramos F. C., Wolff J. A. and Tollstrup D. L. (2004) Measuring $^{87}Sr/^{86}Sr$ variations in minerals and groundmass from basalts using LA-MC-ICP-MS. *Chem. Geol.* **211**, 135–158.

Ranta E., Stockmann G., Wagner T., Fusswinkel T., Sturkell E., Tollefsen E. and Skelton A. (2018) Fluid-rock reactions in the 1.3 Ga siderite carbonatite of the Gronnedal-Ika alkaline complex, Southwest Greenland. *Contrib. Mineral. Petrol.* **173**, 1–26.

Ray J. S. and Ramesh R. (2000) Rayleigh fractionation of stable isotopes from a multicomponent source. *Geochim. Cosmochim. Acta* **64**, 299–306.

Richet P., Bottinga Y. and Javoy M. (1977) A review of hydrogen, carbon, nitrogen, oxygen, sulfur, and chlorine stable isotope fractionation among gaseous molecules. *Ann. Rev. Earth Planet. Sci.* **5**, 65–101.

Santos R. V. and Clayton R. N. (1995) Variation of oxygen and carbon isotopes in carbonatites: A study of Brazilian alkaline complexes. *Geochim. Cosmochim. Acta* **59**, 1339–1352.

Sheard E. R., Williams-Jones A. E., Heiligmann M., Pederson C. and Trueman D. L. (2012) Controls on the Concentration of Zirconium, Niobium, and the Rare Earth Elements in the Thor Lake Rare Metal Deposit, Northwest Territories, Canada. *Econ. Geol.* **107**, 81–104.

Slezak P. and Spandler C. (2019) Carbonatites as recorders of mantle-derived magmatism and subsequent tectonic events: an example of the Gifford Creek carbonatite complex, Western Australia. *Lithos* **328–329**, 212–227.

Slezak P. and Spandler C. (2020) Petrogenesis of the Gifford Creek carbonatite complex, Western Austraalia. *Contrib. Mineral. Petr.* **175**, 28. https://doi.org/10.1007/s00410-020-1666-3.

Smith M. P., Henderson P. and Campbell L. S. (2000) Fractionation of the REE during hydrothermal processes: constraints from the Bayan Obo Fe–REE–Nb deposit, Inner Mongolia, China. *Geochim. Cosmochim. Acta* **64**, 3141–3160.

Smith M. P., Moore K., Kavecsánszki D., Finch A. A., Kynicky J. and Wall F. (2016) From mantle to critical zone: A review of large and giant sized deposits of the rare earth elements. *Geosci. Front.* **7**, 315–334.

Song W., Xu C. and Smith M. P. (2018) Genesis of the world's largest rare earth element deposit, Bayan Obo, China: Protracted mineralization evolution over ~1 b.y. *Geology.* **46**, 323–326.

Su J. H., Zhao X. F., Li X. C., Hu W., Chen M. and Xiong Y. L. (2019) Geological and geochemical characteristics of the Miaoya syenite-carbonatite complex, Central China: Implications for the origin of REE-Nb-enriched carbonatite. *Ore Geol. Rev.* **113**, 103101.

Taylor H. P., Frechen J. and Degens E. T. (1967) Oxygen and carbon isotope studies of carbonatites from the Laacher See district, West Germany and the Alnö district, Sweden. *Geochim. Cosmochim. Acta* **31**, 407–430.

Thomson S. N., Gehrels G. E. and Ruiz J. (2012) Routine low-damage apatite U-Pb dating using laser ablation-multicollector-ICPMS. *Geochem. Geophys. Geosyst.* **13**. https://doi.org/10.1029/2011GC003928.

Trofanenko J., Williams-Jones A. E., Simandl G. J. and Migdisov A. A. (2016) The nature and origin of the REE mineralization in the Wicheeda Carbonatite, British Columbia, Canada. *Econ. Geol.* **111**, 199–223.

Wan J., Liu C. X., Yang C., Liu W. L., Li X. W., Fu X. J. and Liu H. X. (2016) Geochemical characteristics and LA-ICP-MS

zircon U-Pb age of the trachytic volcanic rocks in Zhushan area of Southern Qinling Mountains and their significance. *Geol. Bull. China* **35**, 1134–1143 (in Chinese with English abstract).

Wang, G., 2014. Metallogeny of the Mesozoic and Paleozoic volcanic igneous event in Ziyang-Langao areas, North Daba Mountain. Ph. D. thesis. China University of Geosciences, Beijing (in Chinese with English abstract).

Wang R., Xu Z., Santosh M., Liang F. and Fu X. (2017) Petrogenesis and tectonic implications of the Early Paleozoic intermediate and mafic intrusions in the South Qinling Belt, Central China: Constraints from geochemistry, zircon U-Pb geochronology and Hf isotopes. *Tectonophysics* **712–713**, 270–288.

Weng Z., Jowitt S. M. and Ansdell K. M. (2015) A detailed assessment of global rare earth element resources: opportunities and challenges. *Econ. Geol.* **110**, 1925–1952.

Williams-Jones A. E., Migdisov A. A. and Samson I. M. (2012) Hydrothermal mobilization of the rare earth elements-a tale of "Ceria" and "Yttria". *Elements* **8**, 355–360.

Wu M., Xu C., Wang L. J. and Song W. L. (2011) A preliminary study on genesis of REE deposit in Miaoya. *Acta Mineral. Sin.* **31**, 478–484 (in Chinese with English abstract).

Wu Y. B. and Zheng Y. F. (2013) Tectonic evolution of a composite collision orogen: an overview on the Qinling-Tongbai-Hong'an-Dabie-Sulu orogenic belt in central China. *Gondwana Res.* **23**, 1402–1428.

Xiang Z., Yan Q., Song B. and Wang Z. (2016) New evidence for the ages ultramafic to mafic dikes and alkaline volcanic complexes in the North Daba Mountains and its geological implication. *Acta Geol. Sin.* **90**, 896–916 (in Chinese with English abstract).

Xie Y. L., Hou Z. Q., Yin S. P., Dominy S. C., Xu J. H., Tian S. H. and Xu W. Y. (2009) Continuous carbonatitic melt-fluid evolution of a REE mineralization system: Evidence from inclusions in the Maoniuping REE deposit, Western Sichuan, China. *Ore Geol. Rev.* **36**, 90–105.

Xu C., Chakhmouradian A. R., Taylor R. N., Kynicky J., Li W. B., Song W. L. and Fletcher I. R. (2014) Origin of carbonatites in the south Qinling orogen: implications for crustal recycling and timing of collision between the South and North China blocks. *Geochim. Cosmochim. Acta* **143**, 189–206.

Xu C., Kynicky J., Chakhmouradian A. R., Campbell I. H. and Allen C. M. (2010) Trace-element modeling of the magmatic evolution of rare-earth-rich carbonatite from the Miaoya deposit, Central China. *Lithos* **118**, 145–155.

Xu C., Kynicky J., Chakhmouradian A. R., Li X. H. and Song W. L. (2015) A case example of the importance of multi-analytical approach in deciphering carbonatite petrogenesis in South Qinling orogen: Miaoya rare-metal deposit, central China. *Lithos* **227**, 107–121.

Xue S., Ling M. X., Liu Y. L., Kang Q. Q., Huang R. F., Zhang Z. K. and Sun W. D. (2020) The formation of the giant Huayangchuan U-Nb deposit associated with carbonatite in the Qinling Orogenic Belt. *Ore Geol. Rev.* **122**, 103498. https://doi.org/10.1016/j.oregeorev.2020.103498.

Xue S., Ling M. X., Liu Y. L. and Sun W. D. (2018) Recycling of subducted carbonates: Formation of the Taohuala Mountain carbonatite, North China Craton. *Chem. Geol.* **478**, 89–101.

Yang K. F., Fan H. R., Pirajno F. and Li X. C. (2019) The Bayan Obo (China) giant REE accumulation conundrum elucidated by intense magmatic differentiation of carbonatite. *Geology* **47**, 1198–1202.

Yang X. Y., Lai X. D., Pirajno F., Liu Y. L., Mingxing L. and Sun W. D. (2017) Genesis of the Bayan Obo Fe-REE-Nb formation in Inner Mongolia, North China Craton: A perspective review. *Precambrian Res.* **288**, 39–71.

Ying Y. C., Chen W., Lu J., Jiang S. Y. and Yang Y. H. (2017) In situ U-Th-Pb ages of the Miaoya carbonatite complex in the South Qinling orogenic belt, central China. *Lithos* **290–291**, 159–171.

Zhang C. L., Shan G., Yuan H. L., Zhang G. W., Yan Y. X., Luo J. L. and Luo J. H. (2007) Sr-Nd-Pb isotopes of the early paleozoic mafic-ultramafic dykes and basalts from south Qinling belt and their implications for mantle composition. *Sci. China* **50**, 1293–1301.

Zhang D., Liu Y., Pan J., Dai T. and Bayless R. C. (2019a) Mineralogical and geochemical characteristics of the Miaoya REE prospect, Qinling orogenic Belt, China: Insights from Sr-Nd-C-O isotopes and LA-ICP-MS mineral chemistry. *Ore Geol. Rev.* **110**, 102932.

Zhang W., Chen W. T., Gao J. F., Chen H. K. and Li J. H. (2019b) Two episodes of REE mineralization in the Qinling Orogenic Belt, Central China: in-situ U-Th-Pb dating of bastnäsite and monazite. *Miner. Deposita* **54**, 1265–1280.

Zheng Y. F., Mao J. W., Chen Y. J., Sun W. D., Ni P. and Yang X. Y. (2019) Hydrothermal ore deposits in collisional orogens. *Sci. Bull.* **64**, 205–212.

Zhu J., Wang L. X., Peng S. G., Peng L. H., Wu C. X. and Qiu X. F. (2016) U-Pb zircon age, geochemical and isotopic characteristics of the Miaoya syenite and carbonatite complex, central China. *Geol. J..* https://doi.org/10.1002/gj.2859.

Zi J. W., Gregory C. J., Rasmussen B., Sheppard S. and Muhling J. R. (2017) Using monazite geochronology to test the plume model for carbonatites: The example of Gifford Creek Carbonatite Complex, Australia. *Chem. Geol.* **463**, 50–60.

Associate editor: Weidong Sun